Available online at www.sciencedirect.com

ScienceDirect

Underground Space 26 (2026) 387–411

www.keaipublishing.com/undsp

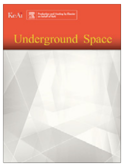

Research Paper

Dynamic response of deep tunnel subjected to contour blasting-unloading considering internal free surface radius

Siyu Peng, Xibing Li *, Lisha Liang, Jingyao Gao

School of Resources and Safety Engineering, Central South University, Changsha 410083, China

Received 24 January 2025; received in revised form 28 August 2025; accepted 22 September 2025
Available online 6 December 2025

Abstract

The dynamic stress response of the surrounding rock in deep tunnels during contour blasting is first derived using elastic statics and dynamics theory alongside Fourier transform methods. This solution uniquely accounts for the effects of lateral stress coefficient, blasting loading, two-dimensional unloading, and the redistribution of static stress fields induced by internal free surfaces. Discrete element numerical simulations are also performed and cross-validated with the theoretical model. The study analyzes and discusses the effects of in-situ stress levels, lateral stress coefficients k, and internal radius ratio $\widetilde{r}_0$ (ratio of internal free surface radius to tunnel radius) on the failure characteristics and mechanisms of surrounding rocks. The results indicate that increasing $\widetilde{r}_0$ can reduce the unloading amplitude, thereby decreasing the dynamic circumferential compressive stress and circumferential cracking induced by unloading, especially under high in-situ stress. Under low stress levels, the maximum dynamic radial compressive stress during blasting decreases, reducing radial compression-shear failure. Simultaneously, the dynamic circumferential tensile stress is also reduced, thereby minimizing blasting-induced radial fractures. However, under extreme lateral stress conditions ($k < 0.2$), adjusting $\widetilde{r}_0$ cannot cause the circumferential stress to exceed the radial stress at the tunnel contour along the maximum principal stress direction. As a result, an ideal contour blasting effect cannot be achieved, and failure continues to propagate radially. In conclusion, the derived dynamic blasting-unloading stress response, in relation to the internal radius ratio, provides theoretical analysis tools for understanding the failure characteristics and mechanisms of surrounding rock during contour blasting, serving as a foundation for optimizing blasting and support design.

Keywords: Dynamic response; Contour blasting; Transient unloading; In-situ stress; P-wave and S-wave; Internal radius ratio

1 Introduction

Underground tunnels are widely employed in civil and mining engineering. As shallow resources are progressively depleted, tunnel excavations are increasingly advancing to deeper and ultra-deep depths (Li et al., 2022; H. Zhu et al., 2019). Deep rock is typically hard and subjected to high stresses, including both gravitational and tectonic forces (Li et al., 2017). Consequently, blasting remains the most cost-effective excavation method and continues to be widely employed (Yilmaz & Unlu, 2013). During blasting, deep rock under high static stress forms a free surface due to blasting loading, resulting in in-situ stress unloading and redistribution near the excavated surface (Yang et al., 2018). This differs from shallow geotechnical engineering in rock properties, excavation methods, initial static stresses, and dynamic stress evolution (Liu et al., 2024). These distinctions lead to unique challenges in deep tunnel excavation, including reduced blasting efficiency and the frequent occurrence of geological hazards, such as splitting (Jiang et al., 2013), rockbursts (Zhou et al., 2024), and zonal disintegration (Li et al., 2008). Therefore, investigating the dynamic response of the surrounding rock during deep tunnel excavation has become a critical research topic.

In tunnel contour blasting, smooth blasting and presplitting are widely used controlled blasting techniques that

---

* Corresponding author.
E-mail address: xbli@csu.edu.cn (X. Li).

Peer review under the responsibility of Tongji University

https://doi.org/10.1016/j.undsp.2025.09.005

enhance both blasting efficiency and surrounding rock stability (Bhandari, 1997). The key distinction lies in whether the main blast detonation has already occurred and created a free surface before contour blasting (Li et al., 2024a; Svanholm et al., 1978). The free surface radius before contour blasting critically affects the initial static stress field. As early as 1898, Kirsch derived an elastic statics solution for the stress field around a circular opening in an infinite plane (Kirsch, 1898), demonstrating that significant stress concentration occurs within a range of 1–3 times the cavity radius. Under extreme lateral stress coefficients, the circumferential stress at the tunnel boundary ranges from –1 to 3 times the maximum principal compressive stress. Numerous laboratory experiments (Lin et al., 2015; Zhu et al., 2021; Q. Zhu et al., 2019), numerical simulations (Liang et al., 2024b; Su et al., 2023; J. P. Yang et al., 2017), and field investigations (Feng et al., 2018; Li et al., 2012; Read et al., 1998) have explored the effects of in-situ stress, resulting in several key conclusions: The damaged region exhibits an elongation along the minimum principal stress direction (Zhu et al., 2014). In this direction, the surrounding rock is prone to failure modes such as spalling and V-shaped notches (Si et al., 2022). Additionally, under extreme lateral stress coefficients, radial cracks tend to develop in the surrounding rock along the maximum principal stress direction (Zhu et al., 2022).

Under contour blasting, such a coupled dynamic-static process, the dynamic failure of the surrounding rock is inevitably influenced by the initial static stress. High initial static stress typically suppresses the crack propagation in single-hole blasting (Liu et al., 2024). When the lateral stress coefficient deviates from 1, cracks generated during single or double-hole blasting are inclined to propagate along the maximum principal stress direction (Li et al., 2021, 2018). In contour blasting, the long axis of the blasting damage zone is parallel to the maximum principal stress (Li et al., 2024a). The dynamic unloading of static stress cannot be overlooked when analyzing the surrounding rock response in deep tunnel blasting (Lu et al., 2012). Extreme lateral stress coefficients intensify uneven stress redistribution, generating two-dimensional unloading waves during excavation (Zhao et al., 2023). Higher unloading magnitudes and rates intensify dynamic stress concentrations (Li et al., 2020). Nonlinear unloading paths often cause more severe damage than linear paths (Li et al., 2014). Limited research investigated the dynamic stress of the surrounding rock under multi-hole and multi-stage blasting-unloading along various stress paths. These studies reveal that increasing in-situ stress initially reduces but subsequently expands the surrounding rock damage zone (J. H. Yang et al., 2017). When the lateral stress coefficient deviates from 1 and the stress in a certain direction is relatively low, the damage zone elongates parallel to the maximum principal stress. In this case, linear path assumptions tend to overestimate the damage. Conversely, the damage zone extends perpendicular to the maximum principal stress. In this case, linear path assumptions may underestimate the damage (Peng et al., 2025). In summary, variations in the free face radius before contour blasting alter the static stress redistribution and then influence the subsequent blasting response and two-dimensional stress unloading response of the surrounding rock, thereby affecting the extent and mechanisms of the damage zone. However, comprehensive studies on this remain limited, and further research is essential for guiding blasting and support.

By combining elastic dynamics and Fourier transform methods, this study investigates dynamic stress evolution in the surrounding rock during contour blasting. The analysis accounts for static stress redistribution caused by internal free surfaces and dynamic unloading of the static stress induced by P-waves and S-waves. Additionally, a numerical model of contour blasting-unloading is established using the discrete element method. Through theoretical analysis, numerical simulations, and laboratory experiments, the effects of contour blasting on the dynamic stress and failure mechanisms of the surrounding rock under different lateral stress coefficients and internal radius ratios are analyzed and discussed.

2 Dynamic theoretical analysis method for contour blasting-unloading by the Fourier transform

2.1 Model assumptions

In this section, a theoretical dynamic model is developed to solve the dynamic stress of the surrounding rock during contour blasting-unloading. Blastholes in circular tunnels are usually arranged in concentric circles within the tunnel boundary, as depicted in Fig. 1(a). The horizontal and vertical principal stresses are P_0 for hydrostatic stresses, and P_0 represents only the vertical principal stresses when discussing non-hydrostatic stresses later. The blasting excavation of a tunnel with a radius of a along principal stresses can be reduced to a plane strain model, as depicted in Fig. 1 (b). This mechanical model adequately represents both types of contour blasting. The r_0 represents the radius of the internal free surface formed by the completed blasting or drilling prior to contour blasting. When r_0 is zero, the model characterizes presplit blasting. Conversely, when r_0 is nonzero, the model describes smooth blasting, with the free surface at r_0 formed by the cutting or main blasting. The internal radius ratio, denoted by $\tilde{r}_0$, is defined as the ratio of r_0 to a. Before contour blasting, the stresses on the tunnel boundary result from the static stress redistribution induced by the internal free surface with a radius of r_0. All blastholes at the boundary are assumed to detonate simultaneously, producing identical stress waves. As displayed in Fig. 1(c), the blasting stress in the adjacent blastholes promotes crack propagation and coalescence, connecting these blastholes along the tunnel contour (Yang et al., 2018). The processes of static stress release and blasting pressure dissipation are interconnected (Peng et al., 2025). For simplicity, the blasting and unloading

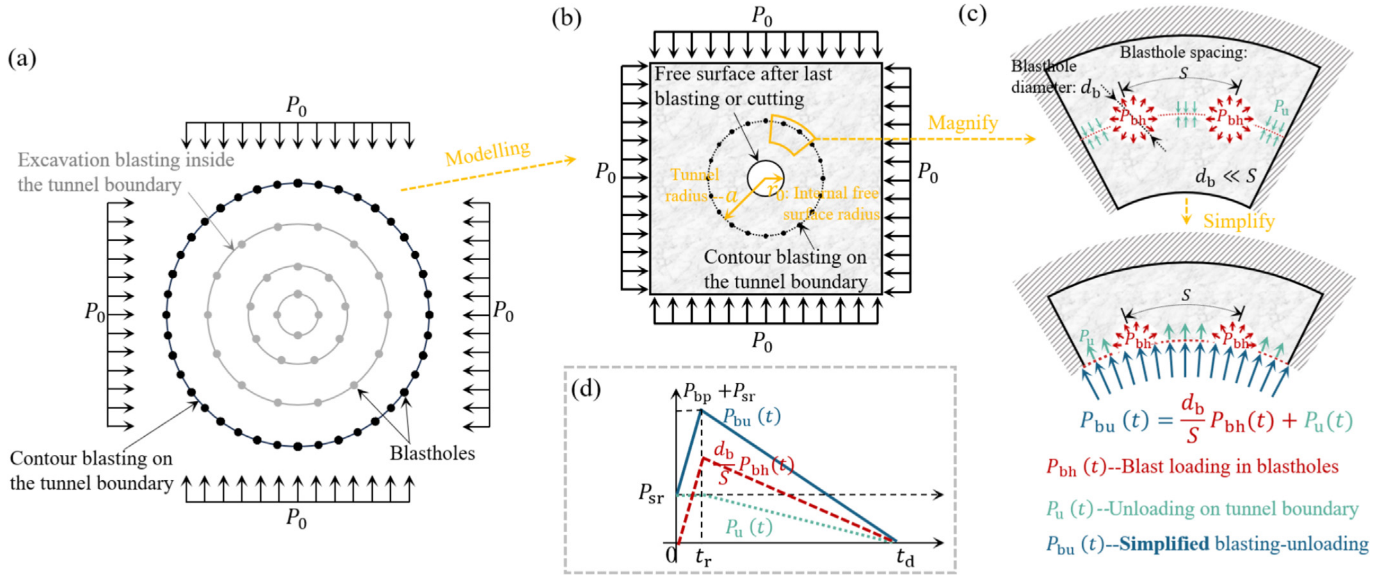

Fig. 1. Mechanical models and simplifications. (a) A typical spatial distribution of blastholes, (b) a mechanical model for contour blasting, (c) its simplifications of blasting and unloading, and (d) the stress paths.

waves are typically described by triangular and linear paths (Li & Li, 2018; Li et al., 2020), respectively, as shown in Fig. 1(d). The stress-time function of simplified blasting-unloading $P_{bu}(t)$ is represented as

$$P_{bu}(t) = \begin{cases} \frac{t}{t_r} P_{bp} + P_{sr} & (0 \le t < t_r) \\ \frac{t_d - t}{t_d - t_r}\left(P_{bp} + P_{sr}\right) & (t_r \le t \le t_d) \\ 0 & (t > t_d) \end{cases}, \tag{1}$$

where t represents time; t_r refers to the rising duration of blasting pressure, set as 0.2 ms (Yilmaz & Unlu, 2013); t_d represents the duration of the blasting-unloading stress with $t_d = 9.0 t_r$; P_{sr} is the initial static stress to be unloaded on the tunnel boundary; P_{bp} is the blasting pressure peak after averaging over the blasting contour.

Previous theoretical studies have treated the dynamic response induced by blasting waves as a radially symmetric one-dimensional dynamical problem. However, the unloading amplitude is determined by the initial in-situ static stress and the lateral stress coefficient k, defined as the ratio of the horizontal to the vertical principal stress. When $k = 1$, the stress path in any direction can be represented as shown in Fig. 1(d). Conversely, when $k \neq 1$, the initial static stresses in different directions are no longer equal. In this case, this dynamic unloading problem becomes a two-dimensional dynamic problem. The anisotropy of unloading amplitude is significantly influenced by k and the radius of the internal free surface r_0 formed by main blasting.

2.2 Dynamic unloading response

To facilitate the elasticity theory solution, and with reference to the static stress calculation method when $k \neq 1$, the two-dimensional dynamic unloading problem with different r_0, as shown in Fig. 2(a), is decomposed into three components. These components include the static stress shown in Fig. 2(b), the radially symmetric dynamic stress shown in Fig. 2(c), and the dynamic stress with a period of π, as shown in Fig. 2(d), where a is the radius of the tunnel. The total unloading dynamic stress evolution at arbitrary locations (r, θ) can be expressed as follows:

$$\begin{cases} \sigma_{u,rr}(t) = \sigma_{s,rr} + \sigma^{(0)}_{d,rr}(t) + \sigma^{(2)}_{d,rr}(t) \\ \sigma_{u,\theta\theta}(t) = \sigma_{s,\theta\theta} + \sigma^{(0)}_{d,\theta\theta}(t) + \sigma^{(2)}_{d,\theta\theta}(t) \\ \tau_{u,r\theta}(t) = \tau_{u,\theta r}(t) = \tau_{s,r\theta} + \tau^{(0)}_{d,r\theta}(t) + \tau^{(2)}_{d,r\theta}(t) \end{cases} \quad r \ge a, \tag{2}$$

where σ_{rr} and $\sigma_{\theta\theta}$ are the total radial and circumferential normal stresses, respectively; $\tau_{r\theta}$ and $\tau_{\theta r}$ are the corresponding radial and circumferential shear stresses; The subscript u denotes that these stresses occur during the unloading. These unloading-induced stresses can be decomposed into static and dynamic components, indicated by the subscripts s and d, respectively. The unloading-induced dynamic component can be further separated into 0-order and 2-order dynamic components, denoted by the superscripts (0) and (2). The static stress in Fig. 2(b) can be calculated using Kirsch formula (Kirsch, 1898):

$$\begin{cases} \sigma_{s,rr} = P_0\left[\left(\frac{1+k}{2}\right)\left(1 - \frac{r_0^2}{r^2}\right) - \left(\frac{1-k}{2}\right)\left(1 - \frac{r_0^2}{r^2}\right)\left(1 - 3\frac{r_0^2}{r^2}\right)\cos 2\theta\right] \\ \sigma_{s,\theta\theta} = P_0\left[\left(\frac{1+k}{2}\right)\left(1 + \frac{r_0^2}{r^2}\right) + \left(\frac{1-k}{2}\right)\left(1 + 3\frac{r_0^4}{r^4}\right)\cos 2\theta\right] \\ \tau_{s,r\theta} = \tau_{s,\theta r} = P_0\left(\frac{1-k}{2}\right)\left(1 - \frac{r_0^2}{r^2}\right)\left(1 + 3\frac{r_0^2}{r^2}\right)\sin 2\theta \end{cases} \quad r \ge r_0. \tag{3}$$

Building on the prior simplification, solving for the total dynamic unloading response when $k \neq 1$ reduces to determining the 0-order and the 2-order dynamic stresses components. Prior studies have addressed similar dynamic problems using Laplace transforms (Miklowitz, 1978). In this study, the transient-state stress evolution is obtained

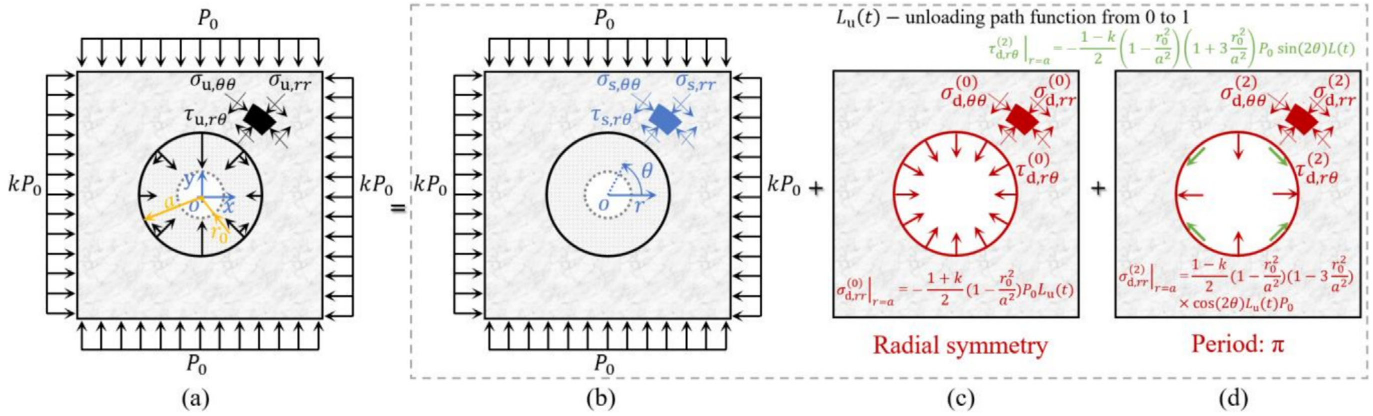

Fig. 2. Dynamic and static stress superposition of tunnel unloading model when $k \neq 1$. (a) Tunnel dynamic unloading, (b) static component, (c) 0-order dynamic component, and (d) 2-order dynamic component.

by superposing the steady-state response according to the Fourier transform (Peng et al., 2024a). Solving for the 0-order dynamic stress component corresponding to Fig. 2 (c) requires first determining the corresponding steady-state solution. The 0-order cylindrical harmonic P-wave radiating from the origin is expressed as

$$\phi^{(0)} = A_0 H_0^{(1)}(\alpha r)\mathrm{e}^{-\mathrm{i}\omega t}, \tag{4}$$

where A_0 represents the wave amplitude; $H_0^{(1)}$ denotes the 0-order Hankel function of the first kind; ω refers to the wave frequency; $\alpha = \omega / c_\mathrm{p}$ is the P-wave number, and c_p is the P-wave velocity. The stress field of 0-order dynamic component around the tunnel is

$$\begin{aligned}\sigma_{rr}^{(0)} &= \lambda\left(\frac{\partial^2\phi^{(0)}}{\partial r^2} + \frac{1}{r}\frac{\partial\phi^{(0)}}{\partial r}\right) + 2\mu\frac{\partial^2\phi^{(0)}}{\partial r^2} \\ &= A_0\left[\mu\alpha^2 H_2^{(1)}(\alpha r) - (\lambda+\mu)\,\alpha^2 H_0^{(1)}(\alpha r)\right]\mathrm{e}^{-\mathrm{i}\omega t},\ (r \geq a),\end{aligned} \tag{5}$$

$$\begin{aligned}\sigma_{\theta\theta}^{(0)} &= \lambda\frac{\partial^2\phi^{(0)}}{\partial r^2} + \frac{1}{r}(\lambda+2\mu)\frac{\partial\phi^{(0)}}{\partial r} \\ &= A_0\left[-\mu\alpha^2 H_2^{(1)}(\alpha r) - (\lambda+\mu)\alpha^2 H_0^{(1)}(\alpha r)\right]\mathrm{e}^{-\mathrm{i}\omega t},\ (r \geq a),\end{aligned} \tag{6}$$

$$\tau_{r\theta}^{(0)} = 0, \tag{7}$$

where λ and μ denote the first and the second Lamé parameters, respectively. Similarly, the 2-order cylindrical harmonic P-wave $\phi^{(2)}$ and SV-wave $\psi^{(2)}$, as shown in Fig. 2 (d), radiating from the origin with an angular period of π can be expressed as

$$\phi^{(2)} = A_2 H_2^{(1)}(\alpha r)\cos(2\theta)\mathrm{e}^{-\mathrm{i}\omega t}, \tag{8}$$

$$\psi^{(2)} = B_2 H_2^{(1)}(\beta r)\sin(2\theta)\mathrm{e}^{-\mathrm{i}\omega t}, \tag{9}$$

where A_2 and B_2 are the amplitude of $\phi^{(2)}$ and $\psi^{(2)}$, respectively, $H_2^{(1)}$ represents the 2-order Hankel function, $\beta = \omega / c_s$ denotes the S-wave number, and c_s is the

$$\begin{aligned}\sigma_{rr}^{(2)} &= \lambda\nabla^2\phi^{(2)} + 2\mu\left(\tfrac{\partial^2\phi^{(2)}}{\partial r^2} - \tfrac{1}{r^2}\tfrac{\partial\psi^{(2)}}{\partial\theta} + \tfrac{1}{r}\tfrac{\partial^2\psi^{(2)}}{\partial r\partial\theta}\right) = \\ &\left\{A_2\left[\tfrac{-2\mu\alpha}{r}H_1^{(1)}(\alpha r) + \tfrac{-(\lambda+2\mu)\alpha^2 r^2 + 12\mu}{r^2}H_2^{(1)}(\alpha r)\right] + B_2\left[\tfrac{4\mu\beta}{r}H_1^{(1)}(\beta r) - \tfrac{12\mu}{r^2}H_2^{(1)}(\beta r)\right]\right\}\cos(2\theta)\mathrm{e}^{-\mathrm{i}\omega t},\end{aligned} \tag{10}$$

$$\begin{aligned}\sigma_{\theta\theta}^{(2)} &= \lambda\nabla^2\phi^{(2)} + 2\mu\left(\tfrac{1}{r}\tfrac{\partial\phi^{(2)}}{\partial r} + \tfrac{1}{r^2}\tfrac{\partial^2\phi^{(2)}}{\partial\theta^2} + \tfrac{1}{r^2}\tfrac{\partial\psi^{(2)}}{\partial\theta} - \tfrac{1}{r}\tfrac{\partial^2\psi^{(2)}}{\partial r\partial\theta}\right) = \\ &\left\{A_2\left[\tfrac{2\mu\alpha}{r}H_1^{(1)}(\alpha r) + \tfrac{-\lambda\alpha^2 r^2 - 12\mu}{r^2}H_2^{(1)}(\alpha r)\right] + B_2\left[-\tfrac{4\mu\beta}{r}H_1^{(1)}(\beta r) + \tfrac{12\mu}{r^2}H_2^{(1)}(\beta r)\right]\right\}\cos(2\theta)\mathrm{e}^{-\mathrm{i}\omega t},\end{aligned} \tag{11}$$

$$\begin{aligned}\tau_{r\theta}^{(2)} &= \mu\left(\tfrac{2}{r}\tfrac{\partial^2\phi^{(2)}}{\partial r\partial\theta} - \tfrac{2}{r^2}\tfrac{\partial\phi^{(2)}}{\partial\theta} + \tfrac{1}{r^2}\tfrac{\partial^2\psi^{(2)}}{\partial\theta^2} - \tfrac{\partial^2\psi^{(2)}}{\partial r^2} + \tfrac{1}{r}\tfrac{\partial\psi^{(2)}}{\partial r}\right) = \\ &\left\{A_2\left[\tfrac{-4\mu\alpha}{r}H_1^{(1)}(\alpha r) + \tfrac{12\mu}{r^2}H_2^{(1)}(\alpha r)\right] + B_2\left[\tfrac{2\mu\beta}{r}H_1^{(1)}(\beta r) + \tfrac{\mu\beta^2 r^2 - 12\mu}{r^2}H_2^{(1)}(\beta r)\right]\right\}\sin(2\theta)\mathrm{e}^{-\mathrm{i}\omega t},\end{aligned} \tag{12}$$

S-wave velocity. The stress field of 2-order dynamic component around the tunnel can be expressed as

$$\nabla^2 = \frac{1}{r}\frac{\partial}{\partial r} + \frac{\partial^2}{\partial r^2} + \frac{1}{r^2}\frac{\partial^2}{\partial \theta^2}. \tag{13}$$

As shown in Fig. 2(d), a difference in r_0 causes the boundary condition to be different, with the following relationship after omitting the time term $\mathrm{e}^{-\mathrm{i}\omega t}$:

$$\frac{\sigma_{rr}^{(2)}\big|_{r=a}}{\sigma_{r\theta}^{(2)}\big|_{r=a}} = -\frac{\left(1-3\widetilde{r}_0^2\right)\cos 2\theta}{\left(1+3\widetilde{r}_0^2\right)\sin 2\theta} = \frac{\left(A_2\varepsilon_{11}^{(2)} + B_2\varepsilon_{12}^{(2)}\right)\cos 2\theta}{\left(A_2\varepsilon_{41}^{(2)} + B_2\varepsilon_{42}^{(2)}\right)\sin 2\theta}, \tag{14}$$

$$\frac{A_2}{B_2} = -\frac{\varepsilon_{12}^{(2)}\left(1+3\widetilde{r}_0^2\right) + \varepsilon_{42}^{(2)}\left(1-3\widetilde{r}_0^2\right)}{\varepsilon_{11}^{(2)}\left(1+3\widetilde{r}_0^2\right) + \varepsilon_{41}^{(2)}\left(1-3\widetilde{r}_0^2\right)}, \tag{15}$$

$$\varepsilon_{11}^{(2)} = \frac{-2\mu\alpha}{a}H_1^{(1)}(\alpha a) + \frac{-(\lambda+2\mu)\alpha^2a^2 + 12\mu}{a^2}H_2^{(1)}(\alpha a), \tag{16}$$

$$\varepsilon_{12}^{(2)} = \frac{4\mu\beta}{a}H_1^{(1)}(\beta a) - \frac{12\mu}{a^2}H_2^{(1)}(\beta a), \tag{17}$$

$$\varepsilon_{41}^{(2)} = \frac{-4\mu\alpha}{a}H_1^{(1)}(\alpha a) + \frac{12\mu}{a^2}H_2^{(1)}(\alpha a), \tag{18}$$

$$\varepsilon_{42}^{(2)} = \frac{2\mu\beta}{a}H_1^{(1)}(\beta a) + \frac{\mu\beta^2a^2 - 12\mu}{a^2}H_2^{(1)}(\beta a). \tag{19}$$

The 0-order and 2-order stress field around the tunnel induced by unit stress loading at the tunnel boundary can be described as

$$\overline{\sigma_{rr}^{(0)}} = \frac{\sigma_{rr}^{(0)}}{\sigma_{rr}^{(0)}\big|_{r=a}},\ \overline{\sigma_{\theta\theta}^{(0)}} = \frac{\sigma_{\theta\theta}^{(0)}}{\sigma_{rr}^{(0)}\big|_{r=a}},\ \overline{\tau_{r\theta}^{(0)}} = \frac{\tau_{r\theta}^{(0)}}{\sigma_{rr}^{(0)}\big|_{r=a}}, \tag{20}$$

$$\overline{\sigma_{rr}^{(2)}} = \frac{\sigma_{rr}^{(2)}}{\sigma_{rr}^{(2)}\big|_{r=a}},\ \overline{\sigma_{\theta\theta}^{(2)}} = \frac{\sigma_{\theta\theta}^{(2)}}{\sigma_{rr}^{(2)}\big|_{r=a}},\ \overline{\tau_{r\theta}^{(2)}} = \frac{\tau_{r\theta}^{(2)}}{\sigma_{rr}^{(2)}\big|_{r=a}}. \tag{21}$$

By applying the Fourier transform to combine steady-state responses and ensuring the dynamic boundary responses match the target waveform, the transient response under dynamic loading conditions can be derived. The response function for an arbitrary dynamic loading condition may be expressed as

$$g(x,t) = \frac{1}{\sqrt{2\pi}}\int_{-\infty}^{\infty}\chi(x_i,\omega)F(\omega)\mathrm{e}^{-\mathrm{i}\omega t}\mathrm{d}\omega, \tag{22}$$

where $\chi(x_i,\omega)$ represents the system's admittance function, defined as the steady-state response of the system caused by an input function of unit magnitude; $F(\omega)$ corresponds to the Fourier transform of the input function $f(t)$. To facilitate calculation, the transient load can be approximated into a series of pulse functions, and the transient response corresponding to a unit impulse input function is given by

$$g_\delta(x,t) = \frac{2}{\pi}\int_0^\infty R(\omega)\cos(\omega t)\mathrm{d}\omega, \tag{23}$$

where $R(\omega)$ represents the real portion of the admittance function. Based on Duhamel integral and Eq. (23), the transient response for any input function $f(t)$ is expressed as

$$g(x,t) = \int_0^t f(\tau)g_\delta(t-\tau)\mathrm{d}\tau. \tag{24}$$

As shown in Fig. 1(d), the input functions $f(t)$ can be expressed as

$$f(t) = L_\mathrm{u}(t_\mathrm{u}) = \begin{cases} t_\mathrm{u}/(t_\mathrm{d}-t_\mathrm{r}), & 0 \le t_\mathrm{u} < t_\mathrm{d}-t_\mathrm{r} \\ 1, & t_\mathrm{u} > t_\mathrm{d}-t_\mathrm{r} \end{cases}, \tag{25}$$

where $t_\mathrm{u} = t - t_\mathrm{r}$, and $L_\mathrm{u}(t_\mathrm{u})$ is unloading path function. The unloading-induced transient response around the tunnel can be expressed by substituting Eqs. (23) and (25) into Eq. (24) as follows:

$$g_\mathrm{u}(t_\mathrm{u}) = \begin{cases} \frac{2}{\pi(t_\mathrm{d}-t_\mathrm{r})}\int_0^\infty \frac{1-\cos(\omega t_\mathrm{u})}{\omega^2}R(\omega)\mathrm{d}\omega, & 0 \le t_\mathrm{u} < t_\mathrm{d}-t_\mathrm{r} \\ \frac{2}{\pi(t_\mathrm{d}-t_\mathrm{r})}\int_0^\infty \frac{\cos[\omega(t_\mathrm{u}-t_\mathrm{d}+t_\mathrm{r})]-\cos(\omega t_\mathrm{u})}{\omega^2}R(\omega)\mathrm{d}\omega, & t_\mathrm{u} \ge t_\mathrm{d}-t_\mathrm{r} \end{cases}, \tag{26}$$

where $R(\omega)$ represents the real part of the frequency response of Eqs. (20) and (21). When $R(\omega)$ represents the real part corresponding to $\overline{\sigma_{rr}^{(0)}}$, $\overline{\sigma_{\theta\theta}^{(0)}}$, and $\overline{\sigma_{r\theta}^{(0)}}$, respectively, then the results of $-g_\mathrm{u}(t_\mathrm{u})(1+k)\left(1-\widetilde{r}_0^2\right)P_0/2$ represent the corresponding transient response $\sigma_{\mathrm{d},rr}^{(0)}(t_\mathrm{u})$, $\sigma_{\mathrm{d},\theta\theta}^{(0)}(t_\mathrm{u})$, and $\sigma_{\mathrm{d},r\theta}^{(0)}(t_\mathrm{u})$. When $R(\omega)$ represents the real part corresponding to $\overline{\sigma_{rr}^{(2)}}$, $\overline{\sigma_{\theta\theta}^{(2)}}$, and $\overline{\sigma_{r\theta}^{(2)}}$, respectively, then the results of $g_\mathrm{u}(t_\mathrm{u})(1-k)\left(1-\widetilde{r}_0^2\right)\left(1-3\widetilde{r}_0^2\right)P_0\cos(2\theta)/2$ represent the corresponding transient response $\sigma_{\mathrm{d},rr}^{(2)}(t_\mathrm{u})$, $\sigma_{\mathrm{d},\theta\theta}^{(2)}(t_\mathrm{u})$, and $\sigma_{\mathrm{d},r\theta}^{(2)}(t_\mathrm{u})\tan(2\theta)$. By substituting the above results and Eq. (3) into Eq. (2), the total unloading response can be obtained, using the trapezoidal integration method due to the difficulties in deriving the theoretical expression of $R(\omega)$.

2.3 Blasting response

In addition to the initial in-situ stress and its unloading response in the contour blast shown in Fig. 1, the dynamic response induced by blasting must also be considered. Similar to the dynamic response due to the cylindrical tensile wave shown in Fig. 2(c), the blasting response can be viewed as the response due to the cylindrical compression wave. The blasting wave is usually simplified to a triangular path:

$$f(t) = L_\mathrm{b}(t) = \begin{cases} \frac{t}{t_\mathrm{r}} & (0 \le t < t_\mathrm{r}) \\ \frac{t_\mathrm{d}-t}{t_\mathrm{d}-t_\mathrm{r}} & (t_\mathrm{r} \le t \le t_\mathrm{d}) \\ 0 & (t > t_\mathrm{d}) \end{cases}, \tag{27}$$

where $L_b(t)$ is the blasting stress path function, the value of which evolves from 0 to 1 and back to 0 over time.

To solve for the blasting-induced transient response $g_b(t)$ of this triangular wave, then the Fourier transform method above is used. By substituting Eqs. (27) and (23) into Eq. (24), the following expression can be obtained:

$$g_{\mathrm{b}}(t)=\begin{cases}\int_0^{\infty}\frac{2R(\omega)[1-\cos(\omega t)]}{\pi\, t_{\mathrm{r}}\omega^2}\mathrm{d}\omega & (0\le t<t_{\mathrm{r}})\\ -\int_0^{\infty}\frac{2R(\omega)\{1-\cos[\omega(t-t_{\mathrm{r}})]\}}{\omega^2\pi\,(t_{\mathrm{d}}-t_{\mathrm{r}})}\mathrm{d}\omega+\int_0^{\infty}\frac{2R(\omega)\{\cos[\omega(t-t_{\mathrm{r}})]-\cos(\omega t)\}}{\omega^2\pi\, t_{\mathrm{r}}}\mathrm{d}\omega & (t_{\mathrm{r}}\le t\le t_{\mathrm{d}})\\ \int_0^{\infty}\frac{2R(\omega)\{\cos[\omega(t-t_{\mathrm{r}})]-\cos[\omega(t-t_{\mathrm{d}})]\}}{\omega^2\pi\,(t_{\mathrm{d}}-t_{\mathrm{r}})}\mathrm{d}\omega-\int_0^{\infty}\frac{2R(\omega)\{\cos(\omega t)-\cos[\omega(t-t_{\mathrm{r}})]\}}{\omega^2\pi\, t_{\mathrm{r}}}\mathrm{d}\omega & (t>t_{\mathrm{d}})\end{cases},\tag{28}$$

where $R(\omega)$ represents the real part of Eq. (20). When $R(\omega)$ represents the real part corresponding to $\overline{\sigma_{rr}^{(0)}}$, $\overline{\sigma_{\theta\theta}^{(0)}}$, and $\overline{\sigma_{r\theta}^{(0)}}$, respectively, then the results of $P_{\mathrm{pb}}g_{\mathrm{b}}(t)$ represent the corresponding transient response $\sigma_{\mathrm{b},rr}(t)$, $\sigma_{\mathrm{b},\theta\theta}(t)$, and $\sigma_{\mathrm{b},r\theta}(t)$ induced by blasting.

3 Theoretical results and analysis

Contour blasting in deep tunnels involves the coupling between high static stresses and dynamic disturbances. This section presents and analyzes theoretical results for initial static stress before contour blasting, the static stress coupled with dynamic unloading, and the static stress coupled with blasting-unloading stress. The rock mass model has a density of 2754 kg/m^3, a Young's modulus of 17.77 GPa, and a Poisson's ratio of 0.21. Considering that the stress field corresponding to a lateral stress coefficient of $1/k$ can be obtained by rotating the results for a lateral stress coefficient of k by 90°, this study focuses only on the cases where $k \le 1$ with P_0 being the maximum principal in-situ stress. And k is also the ratio of minimum to maximum principal in-situ stress.

3.1 Initial static stress

The radius of the completed main blasting zone will significantly alter the initial stress of the tunnel boundary, thereby affecting the contour blasting (Li et al., 2024b). This section calculates and analyzes the static stress concentration at the tunnel contour under different internal radius ratios $\widetilde{r}_0$ and lateral stress coefficients k.

Figure 3 shows the variation of normalized radial and circumferential normal initial static stresses (normalized by P_0) on the sides of the tunnel boundary with the $\widetilde{r}_0 = r_0/a$ under different k. All stresses normalized by P_0 (also the maximum principal stress in this study) will be denoted with a tilde to represent the corresponding normalized stresses. For example, $\widetilde{\sigma}_{\mathrm{s},rr} = \sigma_{\mathrm{s},rr}/P_0$. As shown in Fig. 3(a), when $k = 0$, $\widetilde{\sigma}_{\mathrm{s},rr}$ first increases and then decreases with the increase of $\widetilde{r}_0$. As k gradually increases, $\widetilde{\sigma}_{\mathrm{s},rr}|_{\widetilde{r}_0=0}$ increases and $\widetilde{\sigma}_{\mathrm{s},rr}$ monotonically decreases with $\widetilde{r}_0$. As shown in Fig. 3(b), under any k, $\widetilde{\sigma}_{\mathrm{s},\theta\theta}$ increases

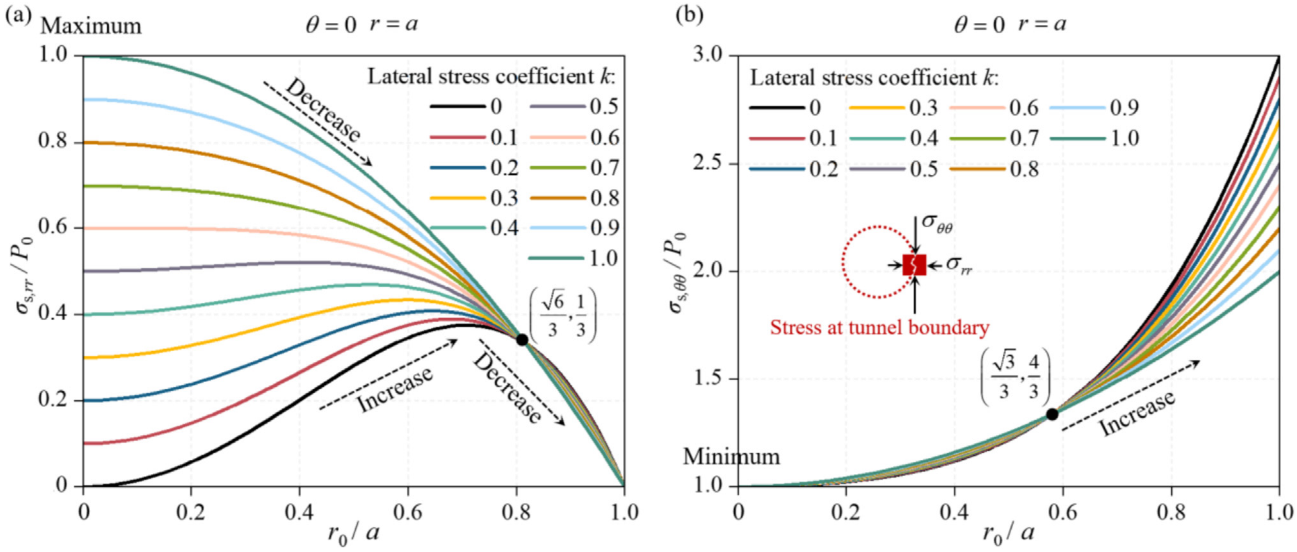

Fig. 3. Initial static stress at the tunnel sidewall ($\theta = 0$, $r = a$) with different $\widetilde{r}_0 = r_0/a$. (a) $\widetilde{\sigma}_{\mathrm{s},rr} = \sigma_{\mathrm{s},rr}/P_0$, and (b) $\widetilde{\sigma}_{\mathrm{s},\theta\theta} = \sigma_{\mathrm{s},\theta\theta}/P_0$.

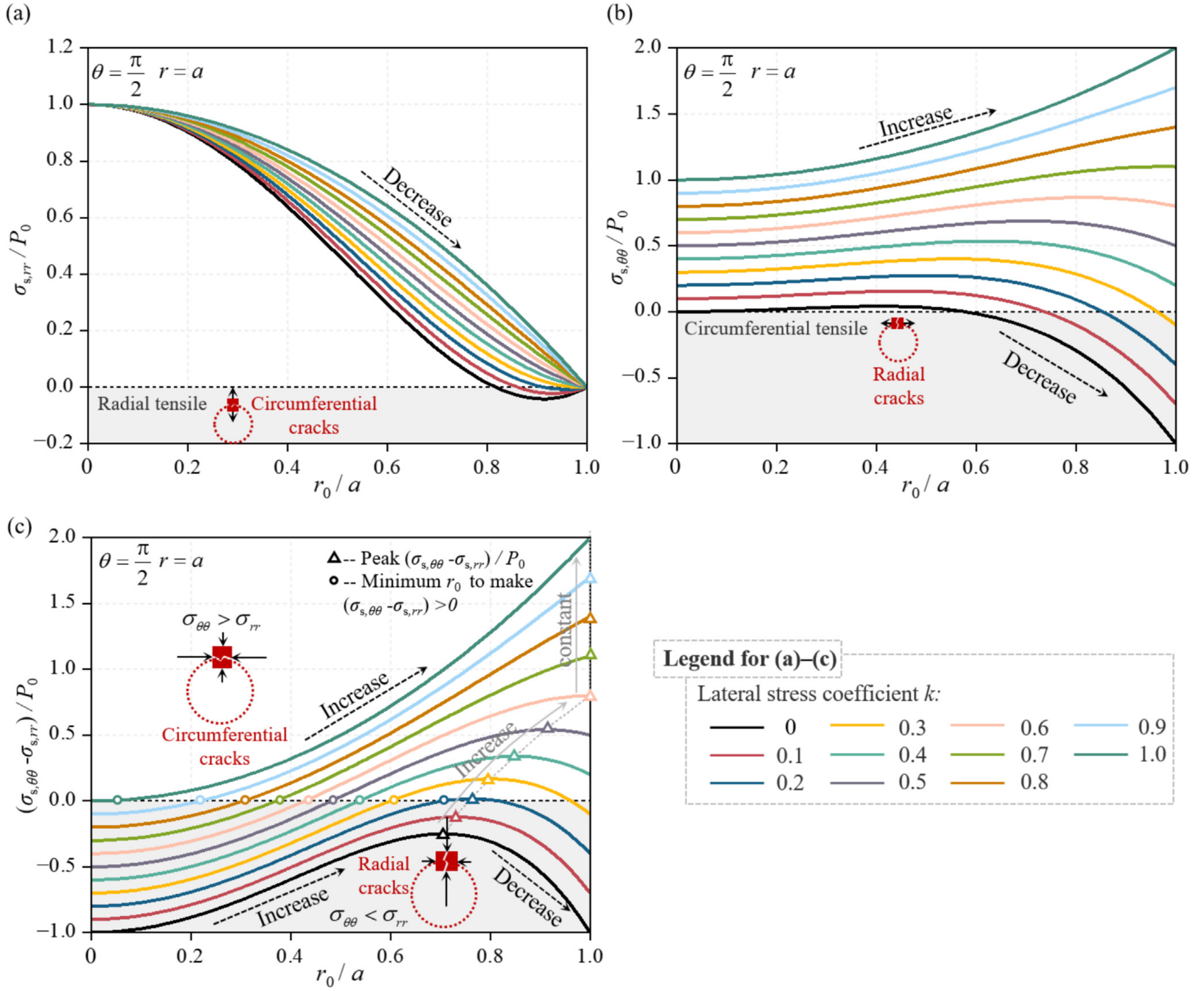

Fig. 4. Initial static stress at the tunnel crown ($\theta = \pi/2, r = a$) with different $\widetilde{r}_0$. (a) $\widetilde{\sigma}_{s,rr} = \sigma_{s,rr}/P_0$, (b) $\widetilde{\sigma}_{s,\theta\theta} = \sigma_{s,\theta\theta}/P_0$, and (c) $\widetilde{\sigma}_{s,\theta\theta} - \widetilde{\sigma}_{s,rr} = (\sigma_{s,\theta\theta} - \sigma_{s,rr})/P_0$.

monotonically with the increase of r_0 and $\widetilde{\sigma}_{s,\theta\theta}|_{\widetilde{r}_0 = 1.0}$ increases linearly with k. According to Eq. (3), when $\widetilde{r}_0$ reaches 0.82, $\widetilde{\sigma}_{s,rr}$ is always less than 0.34. When $\widetilde{r}_0$ reaches 0.58, $\widetilde{\sigma}_{s,\theta\theta}$ is always greater than 1.33. In summary, when $\widetilde{r}_0 \neq 0$, $\widetilde{\sigma}_{s,rr}$ is always smaller than $\widetilde{\sigma}_{s,\theta\theta}$ at the side of the tunnel. As illustrated in Fig. 3(b), increasing $\widetilde{r}_0$ enhances circumferential cracking, leading to smoother tunnel boundaries. This aligns with experimental findings (Li et al., 2024b), where higher stresses parallel to blastholes improve smooth blasting outcomes.

The situation at the tunnel crown is complex. As shown in Fig. 4(a), as $\widetilde{r}_0$ increases, $\widetilde{\sigma}_{s,rr}$ exhibits an overall decreasing trend. Even when $\widetilde{r}_0$ approaches 1 and k approaches 0, $\widetilde{\sigma}_{s,rr}$ remains less than 0. As shown in Fig. 4(b), $\widetilde{\sigma}_{s,\theta\theta}$ increases with an increase in $\widetilde{r}_0$ when $k > 0.5$, and decreases overall with an increase in $\widetilde{r}_0$ when $k < 0.5$. When $\widetilde{\sigma}_{s,\theta\theta}$ is less than $\widetilde{\sigma}_{s,rr}$, this is highly unfavorable for crack connections between the blastholes, hindering the formation of an ideal tunnel contour. Additionally, radial cracks are likely to form and extend into the surrounding rock mass (Li et al., 2024a). From Fig. 4(c), it can be seen that, especially when $k < 0.2$, the ideal static stress conditions for the tunnel crown cannot be achieved under any $\widetilde{r}_0$. As k increases, increasing $\widetilde{r}_0$ can induce a positive value of $(\widetilde{\sigma}_{s,\theta\theta} - \widetilde{\sigma}_{s,rr})$, leading to circumferential cracks. Additionally, the theoretically optimal $\widetilde{r}_0$, corresponding to the peak of $(\widetilde{\sigma}_{s,\theta\theta} - \widetilde{\sigma}_{s,rr})$, initially increases as k increases and then remains constant, and the minimum $\widetilde{r}_0$ to make a positive value of $(\widetilde{\sigma}_{s,\theta\theta} - \widetilde{\sigma}_{s,rr})$ decreases with increasing k.

In conclusion, proper $\widetilde{r}_0$ adjustment can optimize static stress to align crack propagation with tunnel contours under anisotropic stress. However, when $k < 0.2$, this method fails near the boundaries parallel to maximum principal stress, necessitating alternative techniques to enhance circumferential cracking and limit radial crack propagation.

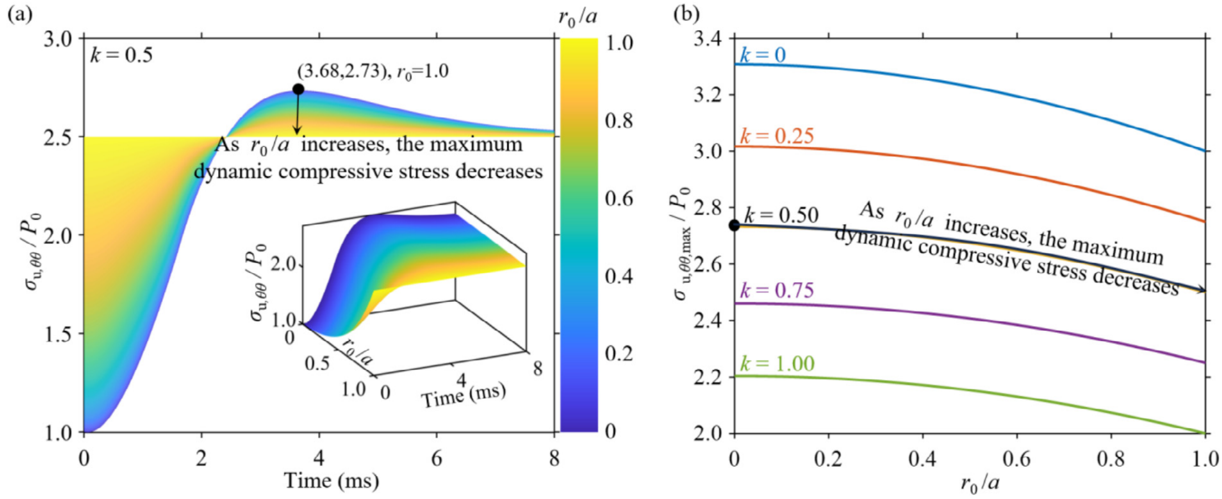

Fig. 5. Dynamic radial normal stress at the tunnel sidewall ($\theta = 0, r = a$) with different $\widetilde{r}_0$ during transient unloading. (a) Stress–time curves under $k = 0.5$, and (b) the peak stress of the stress-time curves under different k.

3.2 Dynamic unloading of static stress

As established previously, variations in $\widetilde{r}_0$ induce the stress redistribution, with k amplifying its anisotropy. This modifies the transient unloading response during contour blasting. This section calculates the dynamic unloading response (as illustrated in Fig. 2) under different $\widetilde{r}_0$.

Figure 5(a) illustrates circumferential stress-time curves at the tunnel sidewall during transient unloading under $k = 0.5$ and varying $\widetilde{r}_0$. For any $\widetilde{r}_0$, the final $\widetilde{\sigma}_{\mathrm{u},\theta\theta}$ stabilizes at 2.5, also the $\widetilde{\sigma}_{\mathrm{u},\theta\theta}|_{\widetilde{r}=1,t=\infty}$, converging to the static solution (Kirsch, 1898). As $\widetilde{r}_0$ increases, $\widetilde{\sigma}_{\mathrm{u},\theta\theta}|_{t=0}$ rises until it reaches the final equilibrium value of 2.5. Correspondingly, the peak of $\widetilde{\sigma}_{\mathrm{u},\theta\theta}$ decreases from 2.73 to 2.50. Different k produce similar dynamic unloading trends shown in Fig. 5(a) but varying dynamic peak and final $\widetilde{\sigma}_{\mathrm{u},\theta\theta}$. Figure 5(b) illustrates the variation of the peak $\widetilde{\sigma}_{\mathrm{u},\theta\theta}$ with $\widetilde{r}_0$ for different k. In conclusion, increasing $\widetilde{r}_0$ reduces dynamic circumferential stress amplitude during transient unloading at sidewalls, mitigating circumferential compression-shear failure.

Figure 6 reveals complex dynamic circumferential stress evolution at the tunnel crown. When $k \leq 0.5$, $\widetilde{\sigma}_{\mathrm{u},\theta\theta}$ at the tunnel crown decreases overall from an initially larger value to a smaller final value, even transitioning from a compressive to a tensile state. In this case, increasing $\widetilde{r}_0$ helps to reduce the amplitude of the additional circumferential tensile stress. In contrast, when $k \geq 0.5$, $\widetilde{\sigma}_{\mathrm{u},\theta\theta}$ redistributes to a larger value, and increasing $\widetilde{r}_0$ can reduce the additional circumferential compressive stress. In conclusion, increasing $\widetilde{r}_0$ always alleviates the dynamic unloading response, aligning with the study result that reducing the unloading amplitude decreases the dynamic response (Li et al., 2020), due to the pre-release of internal strain energy.

3.3 Dynamic response of blasting-unloading

Numerous studies (Li et al., 2021; Tao et al., 2020) have examined dynamic responses around circular cavities under blast loading. Figure 7 presents the dynamic radial and circumferential stress (normalized by P_{bp}) at varying radial distances from the tunnel center. Surrounding rock damage primarily results from dynamic radial compression and circumferential tension, inducing radial crack propagation (Cao & Younis, 2024). While pure blasting creates radially symmetric damage, in-situ stress generates non-circular damage zones (Yi et al., 2018). Under varying $\widetilde{r}_0$, the redistributed static stress field not only affects the amplitude of anisotropic unloading responses but also alters the failure characteristics and mechanisms of surrounding rocks during blasting (Liu et al., 2024). Therefore, blasting dynamic loading, static stress redistribution, and its unloading responses should be considered comprehensively.

The radial stress at the tunnel boundary corresponds to the stress path. Therefore, when $\widetilde{r}_0$ increases, the change in initial radial static stress $\widetilde{\sigma}_{\mathrm{s},rr}$ is consistent with the change in peak radial dynamic stress $\widetilde{\sigma}_{rr,\max}$ under blasting-unloading. Figure 8 shows the dynamic circumstantial stress $\widetilde{\sigma}_{\theta\theta}$ at the tunnel crown under blasting-unloading disturbances for different k and $\widetilde{r}_0$, where $P_{\mathrm{bp}}/P_0 = 2$. When $k = 0$, increasing $\widetilde{r}_0$ increases the circumferential tensile stress. As k increases to 0.5, the effect of $\widetilde{r}_0$ on the dynamic response diminishes, due to the near-constant radial stress before and after blasting. When $k = 1.0$, increasing $\widetilde{r}_0$ reduces the dynamic circumferential tensile stress. Similarly, the dynamic circumferential stress $\widetilde{\sigma}_{\theta\theta}$ at the tunnel sidewall follows the same trend as shown in Fig. 8(c) for any k, which is due to the consistency of the varying unloading amplitudes resulting from changes in $\widetilde{r}_0$ and k, as shown in Fig. 5.

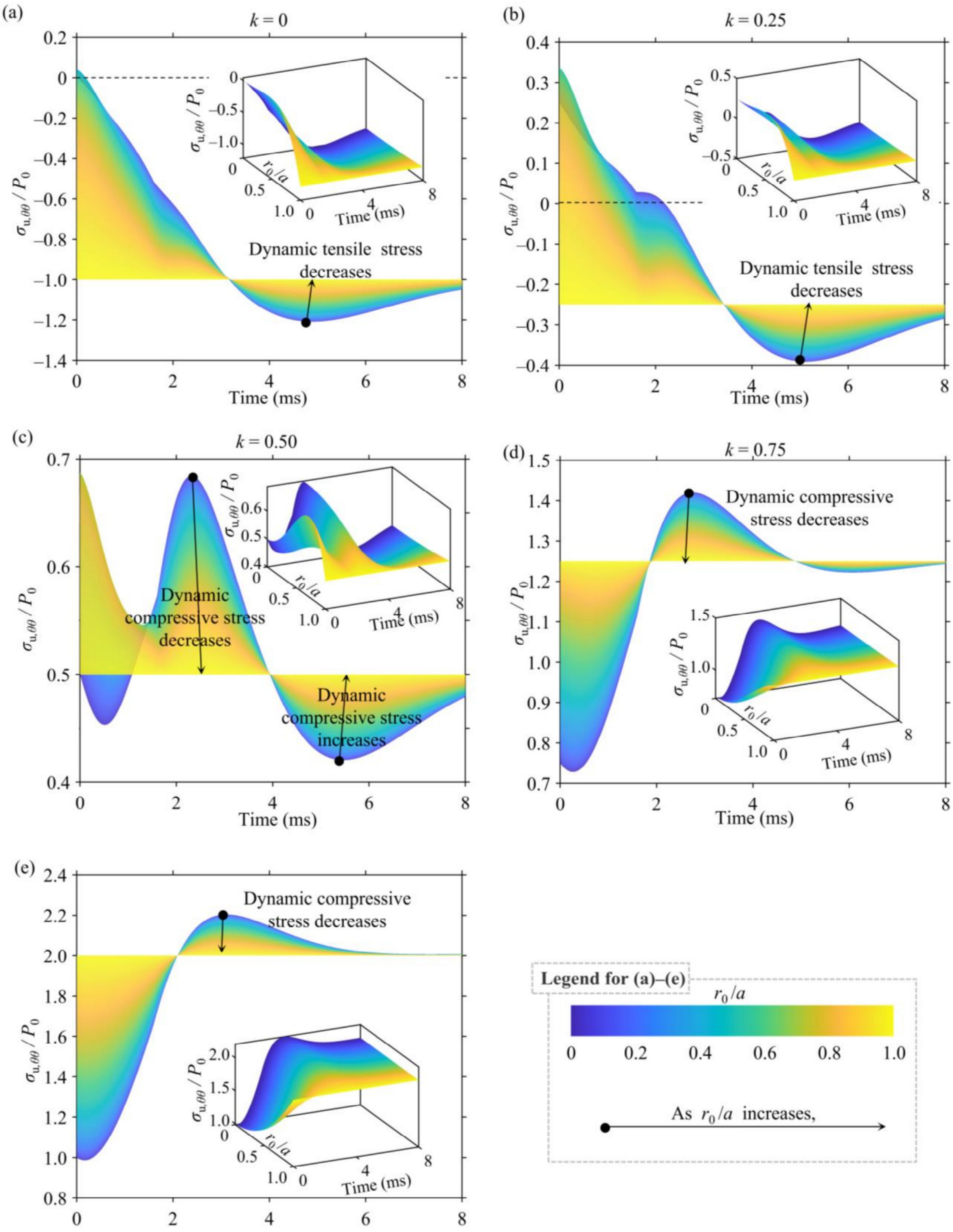

Fig. 6. Dynamic circumferential normal stress at the tunnel crown ($\theta = \pi/2, r = a$) with different $\widetilde{r}_0$ during transient unloading under different k of (a) 0, (b) 0.25, (c) 0.50, (d) 0.75, and (e) 1.00.

Figure 9 illustrates the maximum and minimum dynamic circumferential stresses at the tunnel boundary for different k. In most cases, variations in $\widetilde{r}_0$ have a limited impact on $\widetilde{\sigma}_{\theta\theta,\max}$. Specifically, when $k < 0.5$, a larger $\widetilde{r}_0$ notably reduces the maximum circumferential stress $\widetilde{\sigma}_{\theta\theta,\max}$ at the tunnel crown. Under any k, as shown in

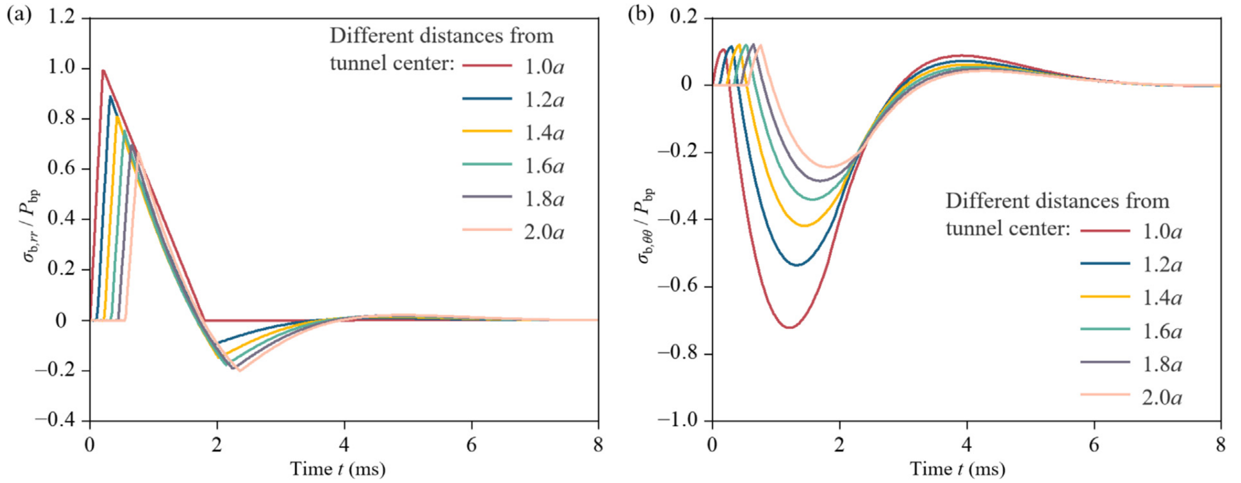

Fig. 7. Dynamic normal stress around the tunnel during blasting. (a) Dynamic radial, and (b) circumferential normal stress.

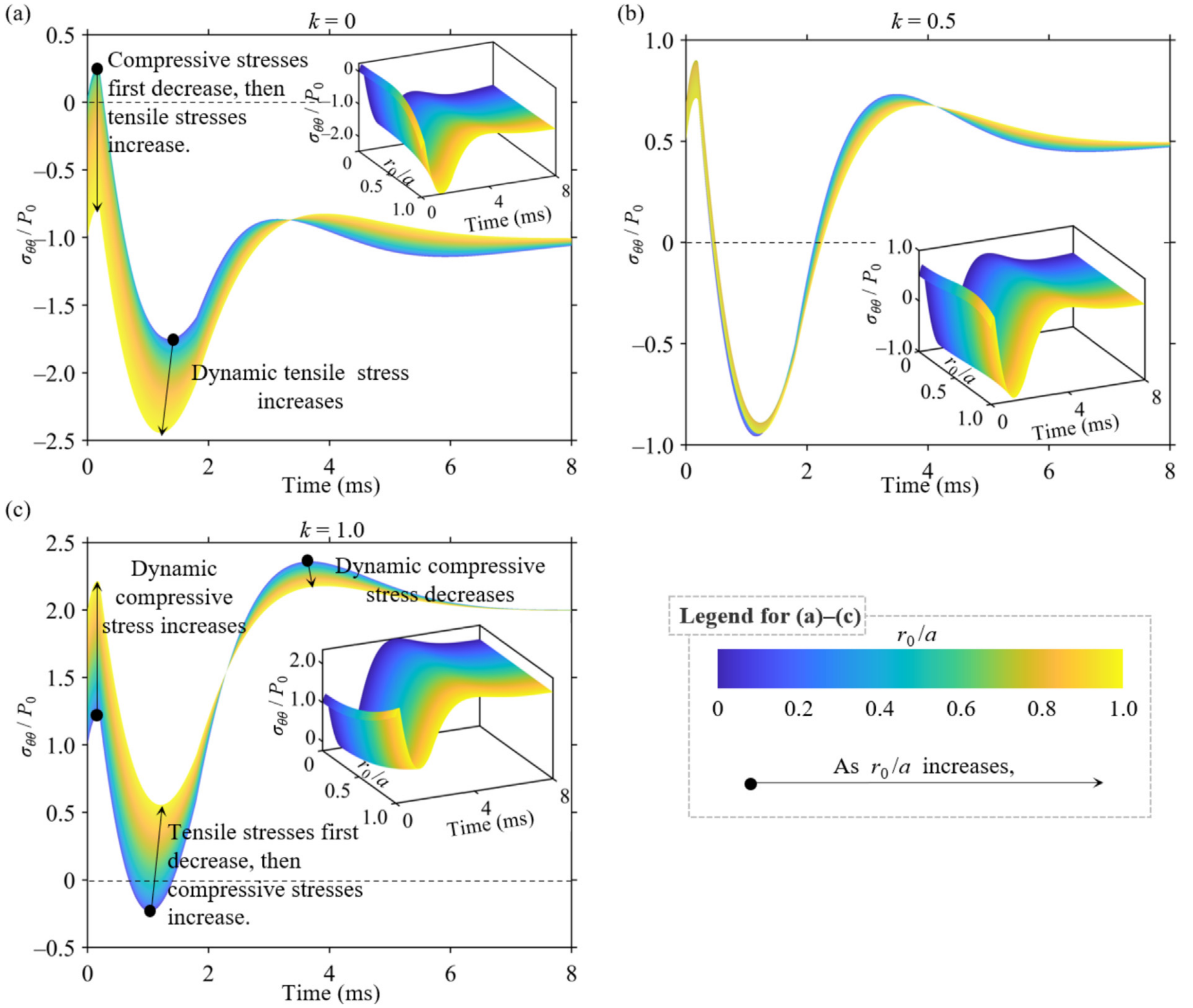

Fig. 8. Dynamic normal stress at the tunnel sidewall ($\theta = \pi/2$, $r = a$) during blasting-unloading under different $\widetilde{r}_0$ and k of (a) 0, (b) 0.5, and (c) 1.0.

Fig. 9(b), increasing $\widetilde{r}_0$ can increase the minimum circumferential tensile stress $\widetilde{\sigma}_{\theta\theta,\min}$ at the tunnel sidewall, eventually transitioning to compressive stress. This proves advantageous in deep hard rock characterized by high compressive-to-tensile stress ratios, effectively mitigating circumferential tensile failure. However, rock failure under

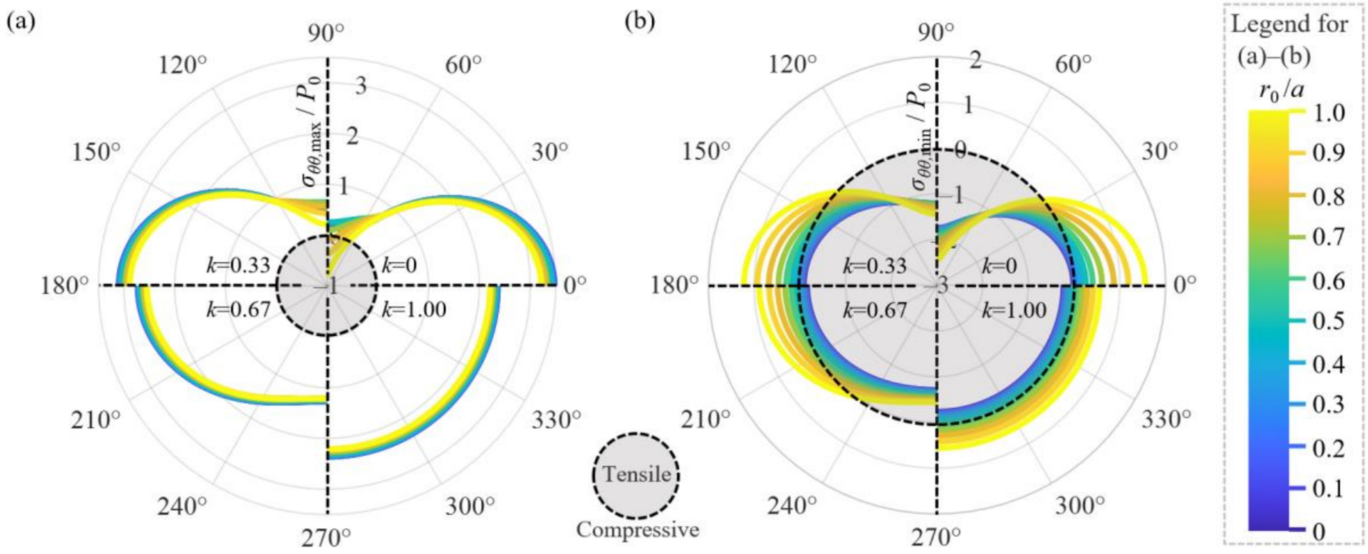

Fig. 9. Extreme values of dynamic circumferential normal stress at the tunnel boundary with different $\tilde{r}_0$ during blasting-unloading under different $k = 0$, 0.33, 0.67, and 1.00. (a) Maximum, and (b) minimum.

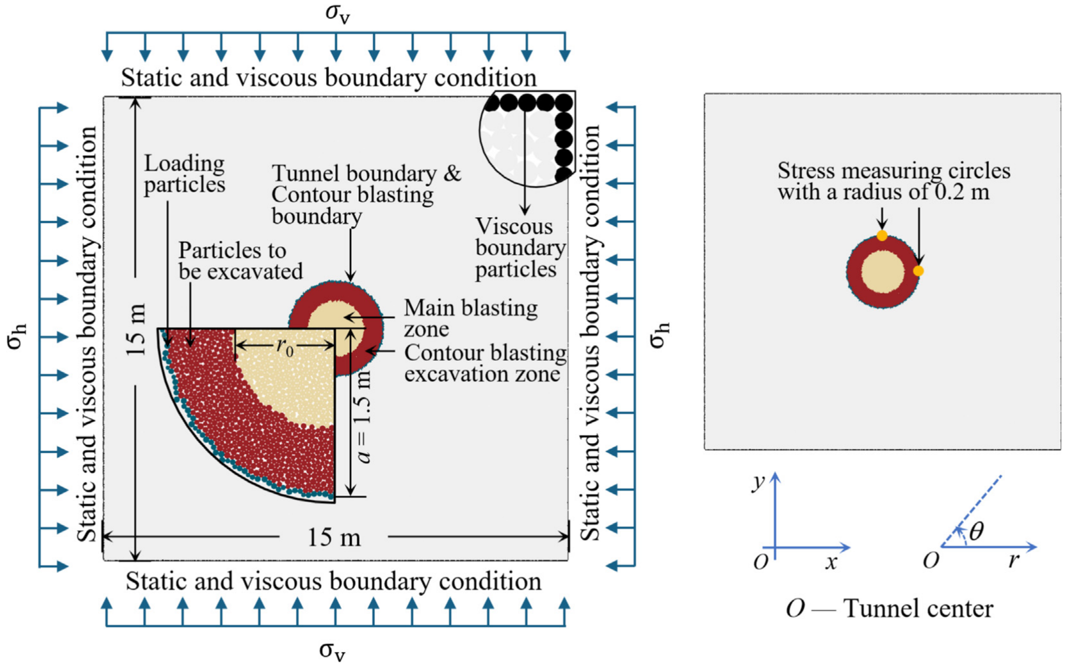

Fig. 10. Discrete element model for tunnel contour blasting.

Table 1
Mechanical parameters of rock mass for calibration and the results (Peng et al., 2025).

Mechanical parameter	Rock mass	Calibrated results	Error (%)
Young's modulus (GPa)	17.71	17.77	0.3
Poisson's ratio	0.22	0.21	4.5
Uniaxial compressive strength (MPa)	90.50	90.57	0.1
Brazilian tensile strength (MPa)	4.36	4.57	4.8
Density (kg/m^3)	2754	2754	0

Table 2
Microscopic parameters of particles and Flat-Joint contacts in PFC (Peng et al., 2024a).

Particle and Flat-Joint contact properties	Value
Modulus (GPa)	16.5
k_n/k_s	2.9
Tensile strength (MPa)	8.5 ± 0.85
Cohesion (MPa)	34.0 ± 3.40
Friction angle (°)	37
Friction coefficient	0.55

two-dimensional dynamic stress states involves complex mechanisms (Peng et al., 2025), necessitating discrete element modeling for accurate failure analysis and validation.

4 Numerical simulations and result analysis

4.1 Numerical model setup

This study establishes a contour blasting-unloading model to investigate rock failure mechanisms using the particle flow code (PFC). Figure 10 shows a 15 m × 15 m model with a 3 m diameter circular tunnel at its center. The model comprises 102 333 particles, with radii ranging from 0.02 to 0.03 m. The physical and mechanical properties of the rock are derived from granite obtained at a depth of 2000 m in the Sanshandao gold mine (Li et al., 2022). Rock mass parameters are derived from laboratory properties using rock quality designation (RQD)-based reduction methods (Peng et al., 2025). Numerical rock models incorporating flat-joint (FJ) contacts are developed for both uniaxial compression and Brazilian splitting simulations to calibrate the microscopic parameters (Peng et al., 2024b). Table 1 lists the calibrated rock mass parameters with <5% deviation from targets. Table 2 presents the corresponding particle and flat-joint contact parameters.

A viscous boundary is used to absorb reflection waves (Peng et al., 2024a), as shown by the black particles in Fig. 10. These particles also serve to apply the in-situ static stress, with vertical principal stress σ_v and horizontal principal stress σ_h imposed by the top/bottom and left/right boundary particles, respectively. Static simulations use 0.7 damping, while dynamic analyses employ zero damping. Figure 11 compares the transmission and reflection characteristics of blasting unloading waves at non-viscous and viscous boundaries, conclusively verifying the necessity and reliability of a viscous boundary. After the viscous boundary configuration, static stress loading is applied until equilibrium is achieved. Subsequently, particles within radius r_0 are removed, followed by stress re-equilibration through forced elastic computation before implementing the failure criteria. The contour blasting simulation is then initiated: (1) recording the unloading forces $F_{u,i}$ exerted by the particles to be excavated on each loading particle i, (2) removing these internal particles while simultaneously applying the recorded forces $F_{u,i}$ to loading particles, (3) resetting accumulated mechanical time to zero, and (4) initiating the blast loading stage by applying the blasting unloading forces $F_{bu,i}$ to each loading particle according to the specified force–time function:

$$F_{bu,i} = \begin{cases} F_{u,i} + 2P_{bp}\frac{\boldsymbol{o}_i}{|\boldsymbol{o}_i|}r_i\frac{t}{t_r} & t \le t_r \\ \left(F_{u,i} + 2P_{bp}\frac{\boldsymbol{o}_i}{|\boldsymbol{o}_i|}r_i\right)\frac{t_d - t}{t_d - t_r} & t_r < t \le t_d\,, \\ 0 & t > t_d \end{cases} \tag{30}$$

where $\frac{\boldsymbol{o}_i}{|\boldsymbol{o}_i|}$ and r_i are the unit position vector and the radius of particle i. The P_{bp} is set as 48.5 MPa, referring to typical blasting parameters applied (Yang et al., 2018).

4.2 Model validation

Contour blasting is implemented using the blasting-induced relaxation excavation method (Peng et al., 2025). The maximum vertical principal stress is set as 50 MPa, based on the in-situ stress conditions at approximately 2000 m depth in the Sanshandao gold mine (Li et al., 2022).

Figure 12 presents state diagrams of models during the simulation of contour blasting with different $\widetilde{r}_0$ under σ_v = 50 MPa and σ_h = 10 MPa ($k = 0.2$). Firstly, the blasting parameters are set, and static stress loading is applied to the model. Second, static excavation is performed within the r_0 region. In this step, the particles within the r_0 region

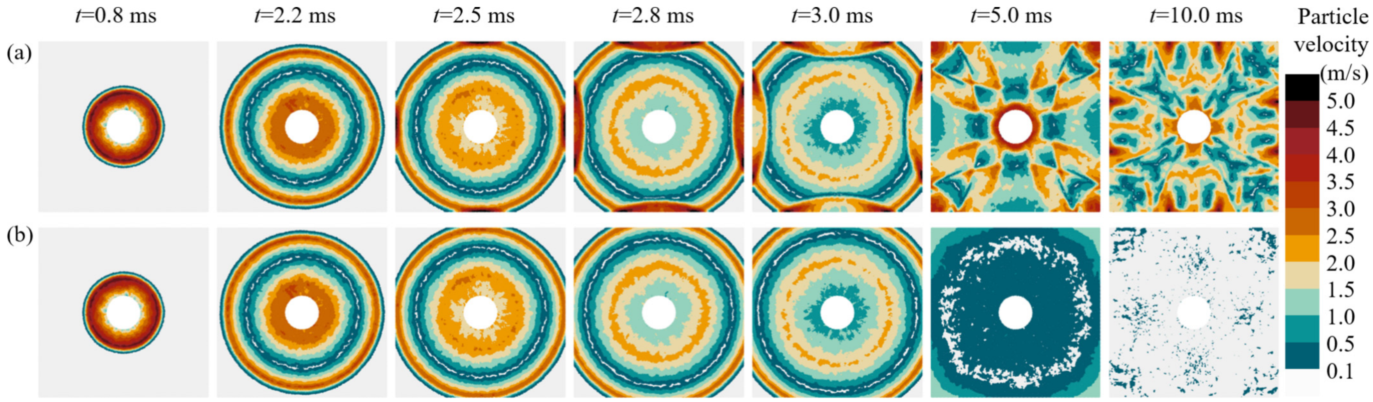

Fig. 11. Transmission and reflection of blasting unloading waves at the (a) non-viscous boundary, and (b) viscous boundary.

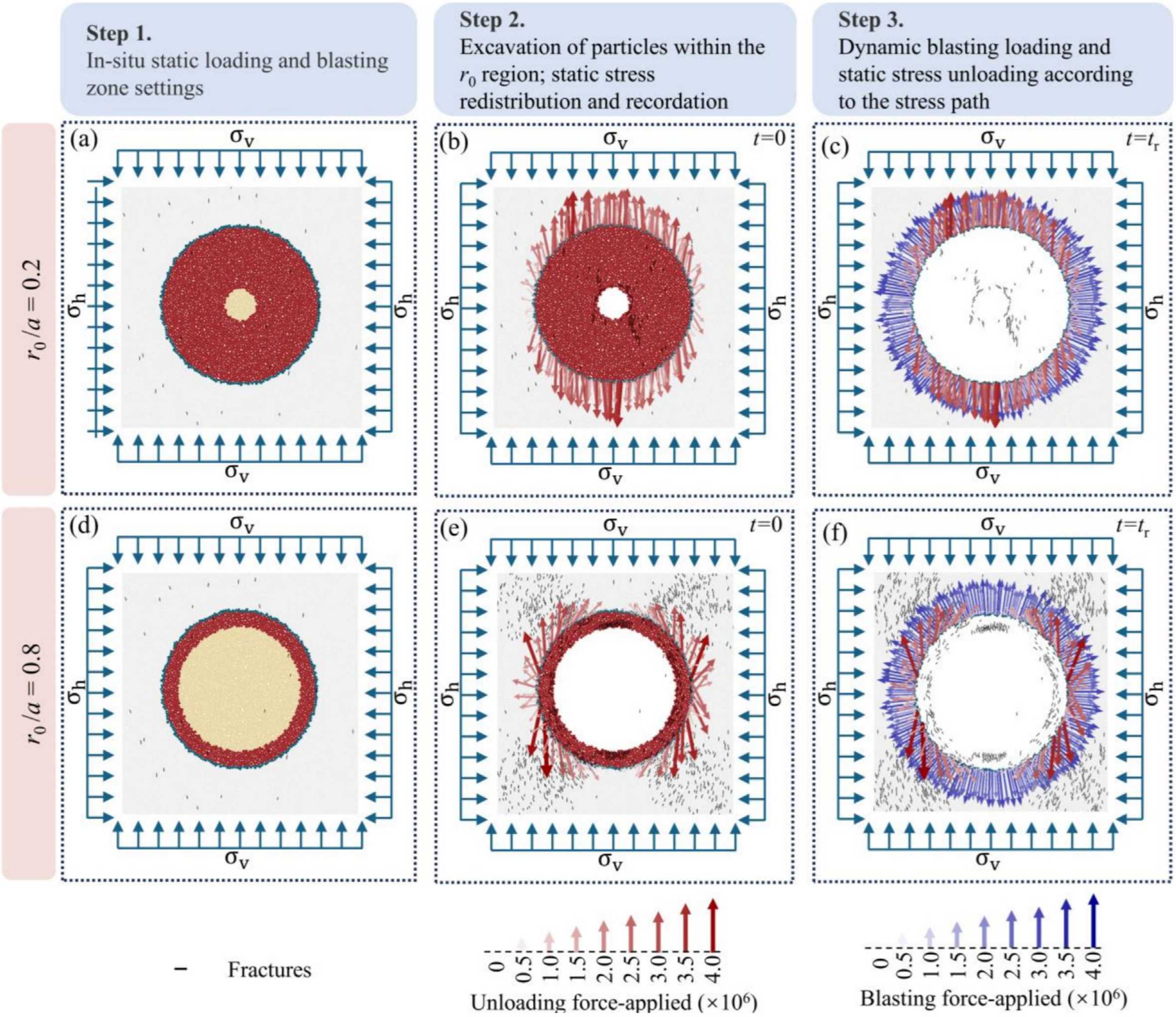

Fig. 12. Diagrams of models during contour blasting simulations with (a)–(c) $\widetilde{r}_0 = 0.2$, and (d)–(f) $\widetilde{r}_0 = 0.8$ under σ_v = 50 MPa and σ_h = 10 MPa ($k = 0.2$).

are removed first, followed by forced elastic calculations until stress equilibrium; then, failure criteria are introduced to ensure that the failure is purely static. After completing Step 2, the static stress field exerted at the tunnel boundary changes due to different r_0. In Fig. 12(b) and (e), the red arrows represent the resultant force acting on each tunnel boundary particle from internal unexcavated rock mass. When $\widetilde{r}_0 = 0.2$, the forces primarily act on the tunnel's upper and lower boundaries. At $\widetilde{r}_0 = 0.8$, the force mainly affects the left and right boundary particles. This force is then applied to the tunnel boundary particles, and internal unexcavated is removed. In Step 3, the blasting pressure is applied according to the stress path. As shown in the blue arrows in Fig. 12(c) and (f), the blasting pressure reaches its peak P_{bp} at $t = t_r$. After $t > t_r$, the blasting pressure and redistributed static stress both unload according to the unloading path function. During this process, the surrounding rock is subjected to dynamic-static combined stresses of varying magnitudes, directions, and paths under different $\widetilde{r}_0$.

Figure 13 shows the dynamic stress at the tunnel boundary from numerical simulations and theoretical solutions, along with the quasi-stress curves calculated under the assumption of linearly increasing excavation radius over time. The dynamic stresses are acquired through measurement circles, with their spatial configuration detailed in Fig. 10. The forced-elastic simulation results in Fig. 13 demonstrate excellent agreement with theoretical predictions, validating the simulation methodology and parameter configuration.

4.3 Analysis of failure characteristics and mechanism

Considering that dynamic stress no longer follows the theoretical stress-time curves once the rock reaches its failure strength (Li et al., 2020), this section analyzes the failure characteristic of the surrounding rock in the conventional simulation (with failure criteria), and combines the results of elastic dynamic theory to explore the failure mechanisms.

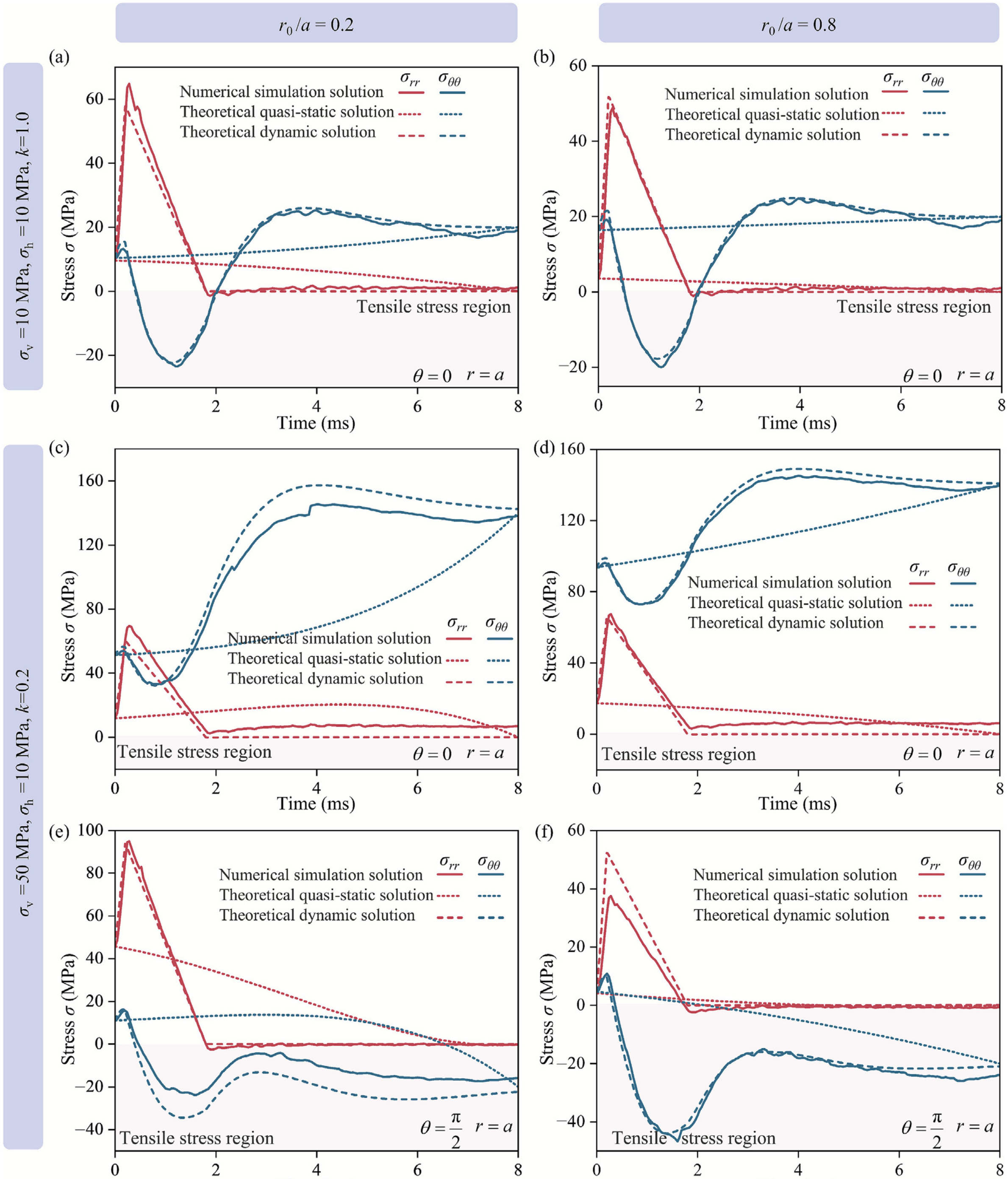

Fig. 13. Validations of theoretical and numerical simulation dynamics stress (without failure criterion calculation).

Figure 14 illustrates the crack distribution in the surrounding rock after contour blasting. The color of the cracks corresponds to the time of their formation. As the stress level increases, the failure extent first contracts and then expands. At low stress level, the cracks are predominantly blue radial fractures formed during the blasting stage. With $\widetilde{r}_0 = 0.8$, both blue radial cracks and red circumferential cracks become less frequent and exhibit limited distribution compared to $\widetilde{r}_0 = 0.2$. Under moderate stress level, orange circumferential cracks formed post-blasting dominate the crack distribution. Blue radial cracks disappear entirely at $\widetilde{r}_0 = 0.8$. While at high stress level, the anisotropy of damage in the surrounding rock becomes more pronounced. As k increases, the total number of cracks initially decreases and subsequently rises. When $k = 0.6$, radial cracks along the direction of the maximum principal stress vanish for $\widetilde{r}_0 = 0.8$ compared to $\widetilde{r}_0 = 0.2$. However, at $k = 0.2$, comparing Fig. 14(i) and (j) reveals

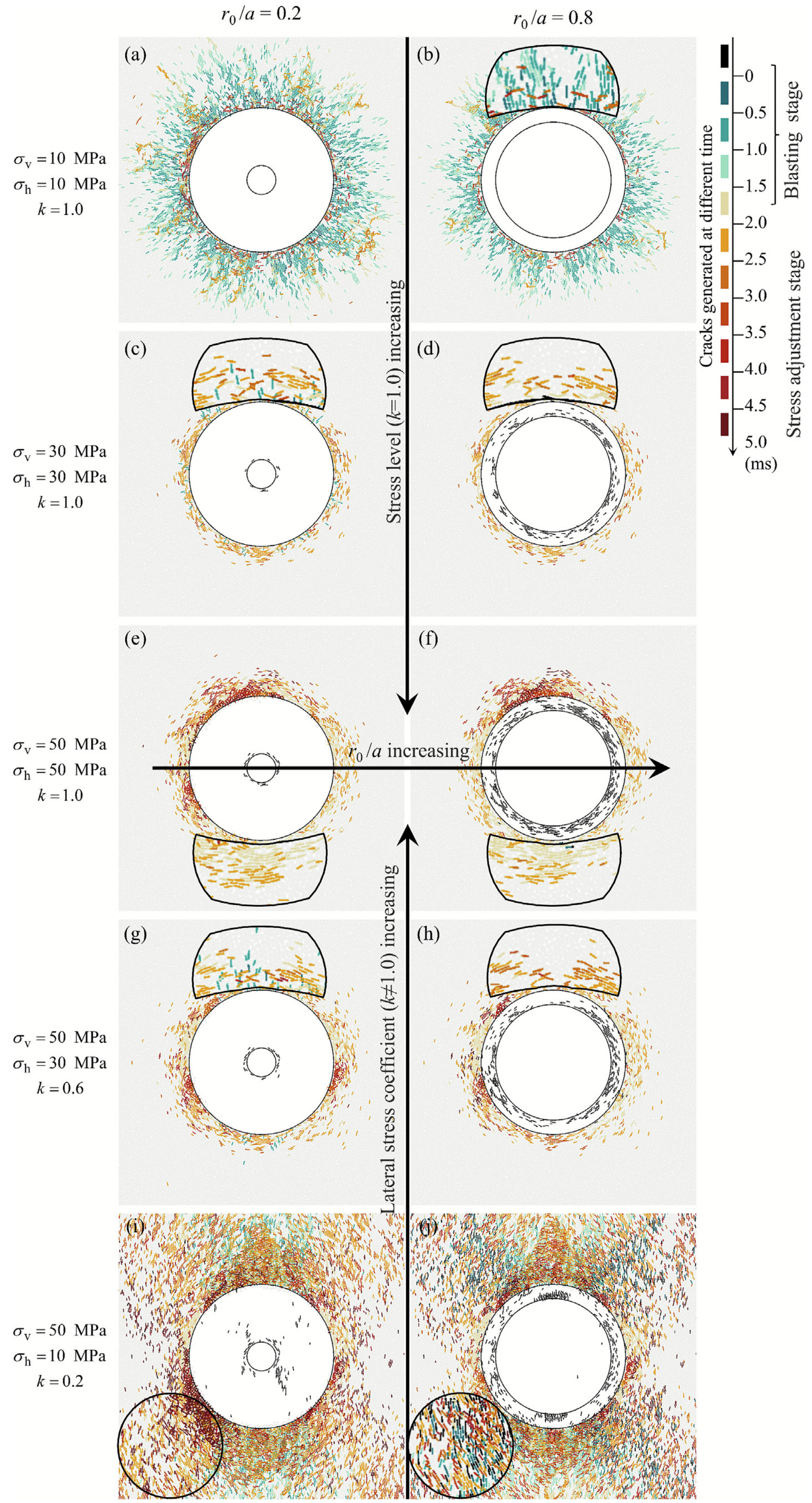

Fig. 14. Fracture map of the surrounding rock during contour blasting with different r_0/a of 0.2 ((a)(c)(e)(g)(i)) and 0.8 ((b)(d)(f)(h)(j)), and under different stress states. (a)(b) $\sigma_v = \sigma_h = 10$ MPa, (c)(d) $\sigma_v = \sigma_h = 30$ MPa, (e)(f) $\sigma_v = \sigma_h = 50$ MPa, (g)(h) $\sigma_v = 50$ MPa and $\sigma_h = 30$ MPa, and (i)(j) $\sigma_v = 50$ MPa and $\sigma_h = 10$ MPa.

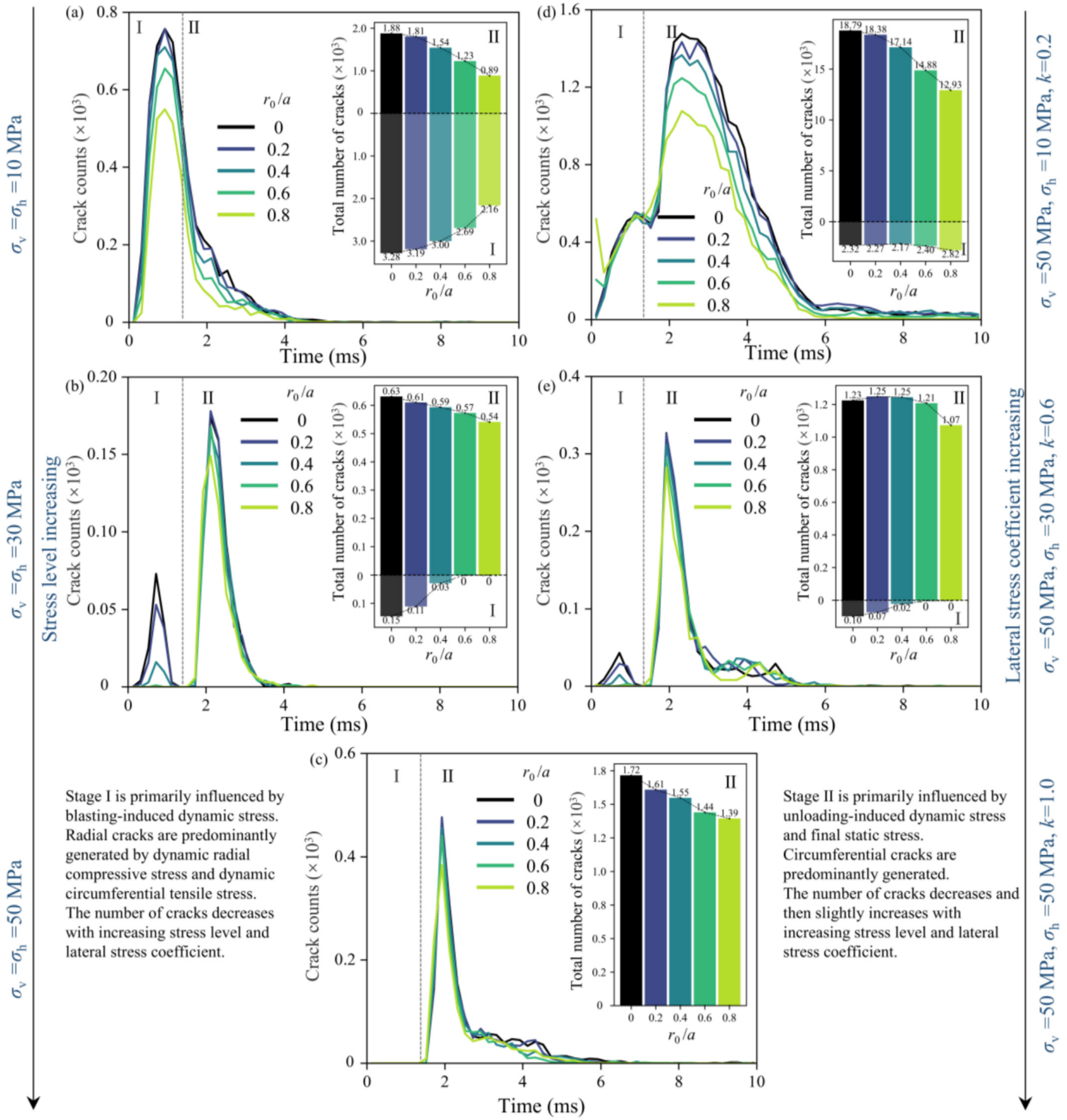

Stage I is primarily influenced by blasting-induced dynamic stress. Radial cracks are predominantly generated by dynamic radial compressive stress and dynamic circumferential tensile stress. The number of cracks decreases with increasing stress level and lateral stress coefficient.

Stage II is primarily influenced by unloading-induced dynamic stress and final static stress. Circumferential cracks are predominantly generated. The number of cracks decreases and then slightly increases with increasing stress level and lateral stress coefficient.

Fig. 15. Variation in crack counts over time with varying $\widetilde{r}_0$ conditions and under different stress states. (a) $\sigma_v = \sigma_h = 10$ MPa, (b) $\sigma_v = \sigma_h = 30$ MPa, (c) $\sigma_v = \sigma_h = 50$ MPa, (d) $\sigma_v = 50$ MPa and $\sigma_h = 10$ MPa, and (e) $\sigma_v = 50$ MPa and $\sigma_h = 30$ MPa.

that more dark blue cracks appear in the x-region surrounding the tunnel when $\widetilde{r}_0 = 0.8$, indicating a more extensive shear stress concentration.

Figure 15 illustrates the variation in crack counts over time at 0.2 ms intervals, under different in-situ stress and varying $\widetilde{r}_0$ conditions. It is evident that the formation of cracks is distinctly divided into two stages. By analyzing the evolution of blasting stress shown in Fig. 7, radial compression and circumferential tension induced by the blast predominantly occur within the first 2 ms, leading to the formation of radial cracks, which is consistent with the analysis in Fig. 14. Therefore, it can be concluded that the cracks observed during the first stages are predominantly driven by the blasting effect. Figure 15(b) and (c)

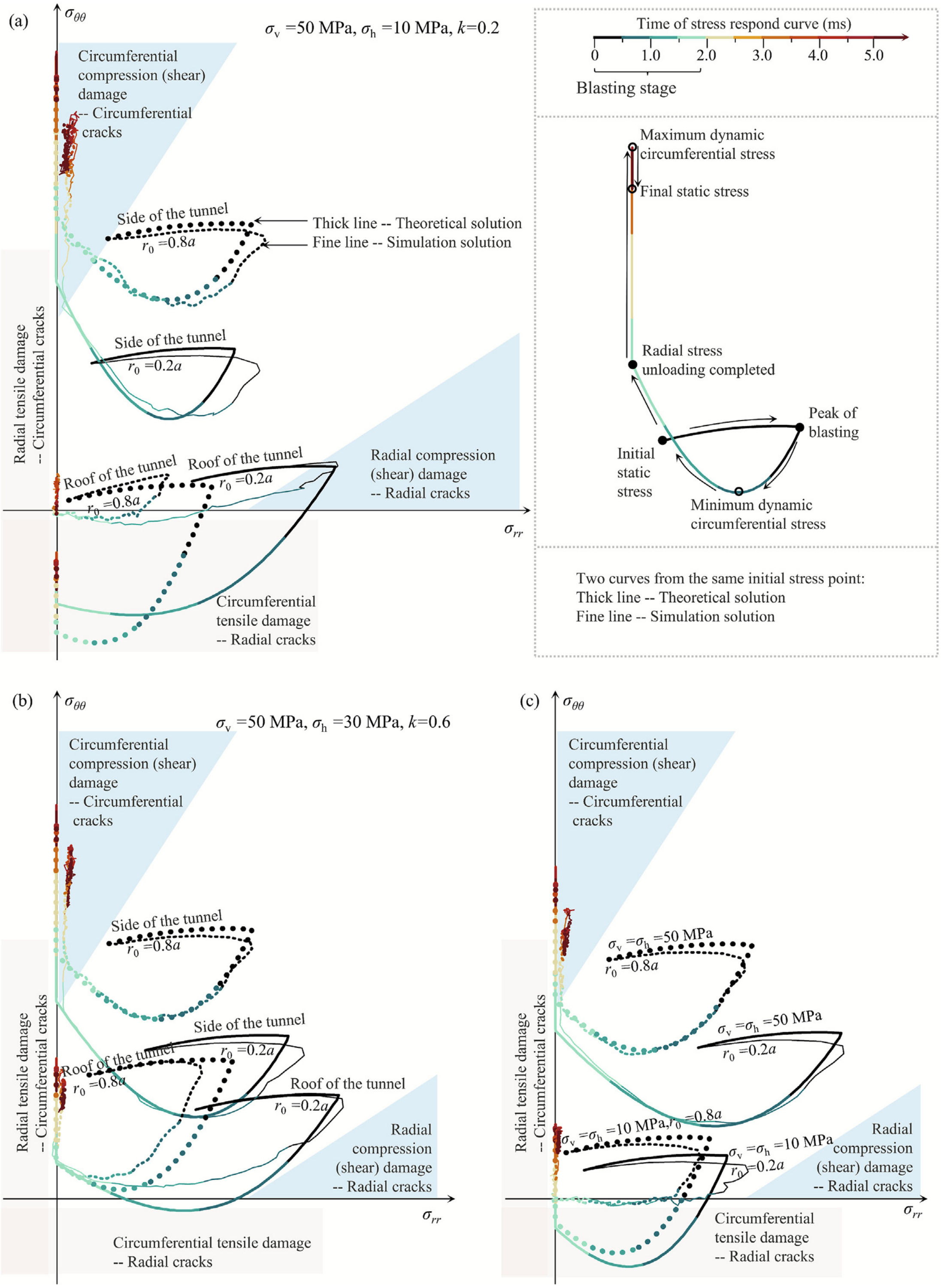

Fig. 16. Dynamic responses of radial and circumferential stresses over time at the tunnel's roof and side, derived from theoretical calculations and simulation results, under varying stress states. (a) $\sigma_v = 50$ MPa and $\sigma_h = 10$ MPa, (b) $\sigma_v = 50$ MPa and $\sigma_h = 30$ MPa, and (c) $\sigma_v = \sigma_h = 50$ MPa and $\sigma_v = \sigma_h = 10$ MPa.

provides a clear division of the time stages, with histograms representing the total crack counts for each stage. The failure trend controlled by blasting or unloading dynamic stresses under this in-situ stress condition is consistent with previous studies (Peng et al., 2025). The primary focus is to examine the effects of variations in $\widetilde{r}_0$. As $\widetilde{r}_0$ increases, the total number of cracks decreases under all in-situ stress conditions. At lower stress levels, as shown in Fig. 15(a), the damage is primarily dominated by blasting effects. In this case, a reduction in $\widetilde{r}_0$, as shown in Fig. 13, decreases maximum dynamic radial compressive stress and circumferential compressive stress, weakening the blast effect. As the stress level increases, as depicted in Fig. 15(c), the failure is primarily governed by unloading and static stress redistribution. A reduction in $\widetilde{r}_0$ decreases the circumferential compressive stress and circumferential cracks, as analyzed in Fig. 6(e). Overall, the damage-reducing effect of increasing $\widetilde{r}_0$ on the surrounding rock diminishes with the increase in the initial in-situ stress. Because dynamic additional compressive stress induced by unloading is limited (Carter & Booker, 1990). When the lateral stress is low, as shown in Fig. 15(d), increasing $\widetilde{r}_0$ leads to more fractures during the first stage but reduces the fractures during the second stage. In this case, the adjustments to dynamic stresses due to varying $\widetilde{r}_0$ exhibit complex variations for different locations in the surrounding rock, resulting in challenges in identifying the specific fracture mechanisms and the stress adjustment mechanisms under different $\widetilde{r}_0$ conditions.

To address this analysis challenge, Fig. 16 presents the radial and circumferential stresses evolution (also the local maximum or minimum principal stresses) over time at the tunnel's roof and side, as obtained from both theoretical calculations and simulation results. Based on the rock properties, the regions of tensile stress-induced cracks (pink areas) and compressive stress-induced cracks (blue areas) are identified (Goodman, 1991; Zhao et al., 2023). The crack directions and failure mechanisms are distinguished by the evolution of radial and circumferential stresses. As illustrated in Fig. 16(a), under σ_v = 50 MPa and σ_h = 10-MPa, the damage on the tunnel's side is primarily caused by circumferential compression-shear failure. Increasing $\widetilde{r}_0$ reduces the maximum dynamic circumferential stress, slightly decreasing circumferential cracks on both sides. For the tunnel roof, when $\widetilde{r}_0 = 0.2$, the peak radial stress induced by blasting, combined with the static stress, results in radial compression-shear failure. In contrast, when $\widetilde{r}_0 = 0.8$, the blasting peak stress no longer enters the radial compression-shear failure region. In addition, at the tunnel roof, the minimum dynamic circumferential stress enters the tensile failure region. Although the theoretical additional circumferential tensile stress for $\widetilde{r}_0 = 0.2$ exceeds that for $\widetilde{r}_0 = 0.8$, the circumferential tensile stress in the surrounding rock does not increase once the tensile strength is exceeded (as shown by the numerical simulation results). In this case, the greater the radial compressive stress, the more intense the resulting tensile failure. Similarly, under σ_v = 50 MPa and σ_h = 30 MPa, the fracture mechanisms in response to changes in $\widetilde{r}_0$ can be clearly identified through Figs. 16(b), 15(e), 14(g), and 14(h).

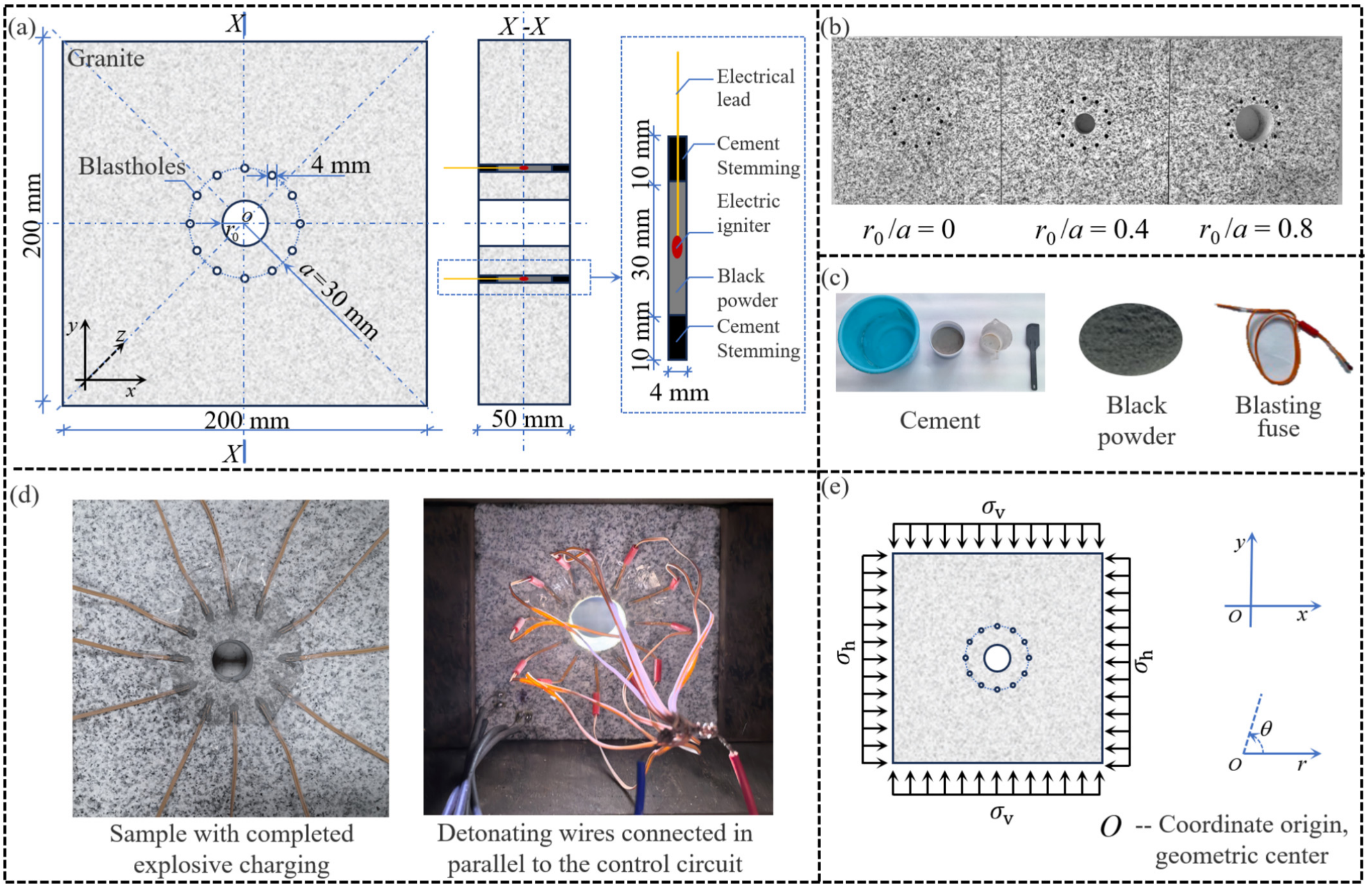

Fig. 17. Specimen preparation instructions. (a) Dimensions of the specimen and charging structure of the blastholes, (b) photos of the specimen, (c) the charging materials, (d) prepared specimens, and (e) schematic of stresses and coordinate axes.

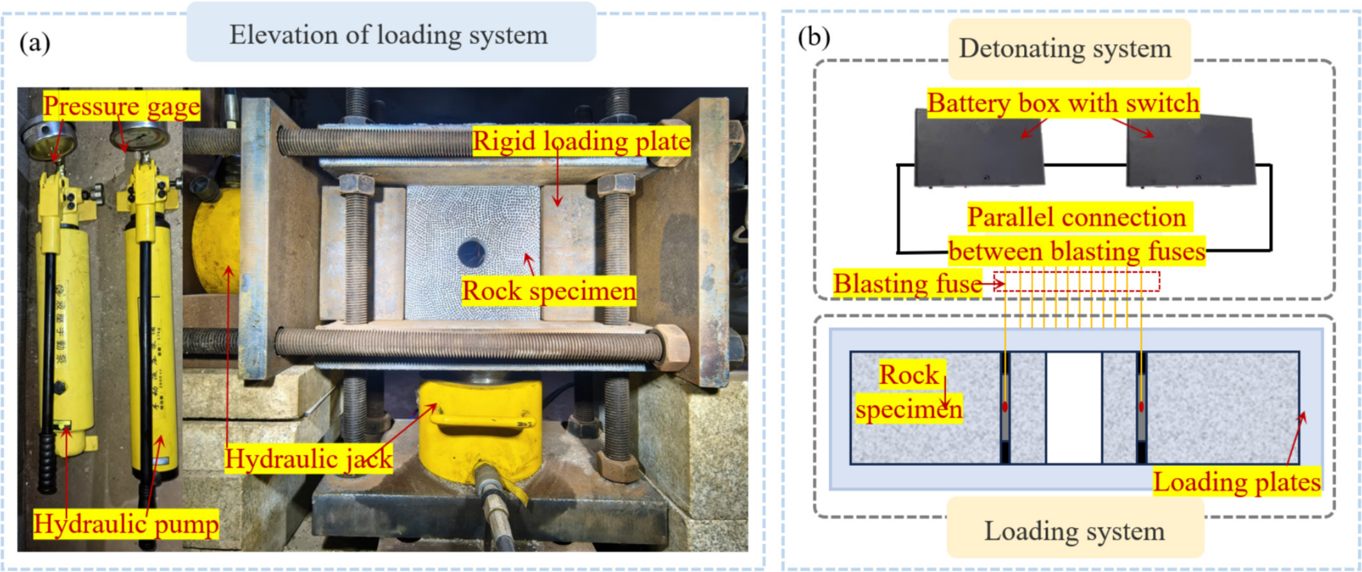

Fig. 18. Experimental apparatus and design. (a) Configuration of the loading system, and (b) loading and the detonating systems.

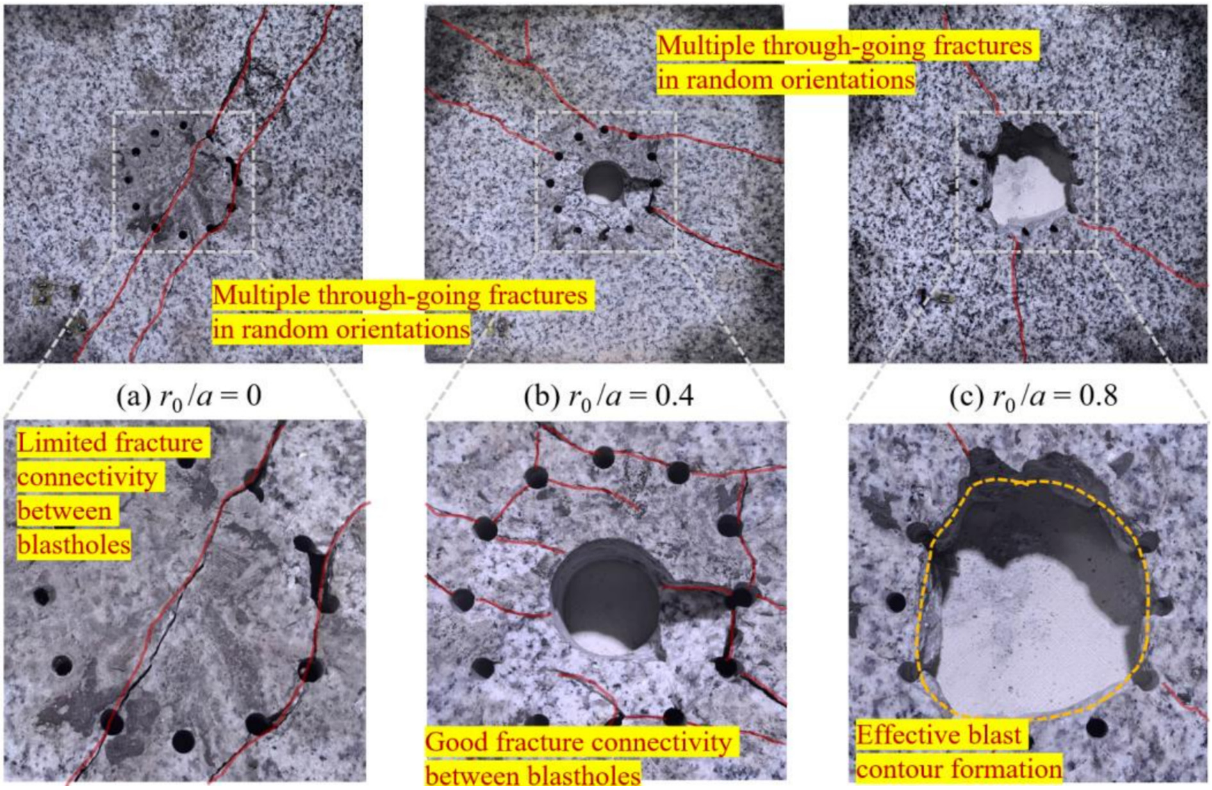

Fig. 19. Failure patterns after blasting under $\sigma_v = 0$ MPa and $\sigma_h = 0$ MPa with different internal radius ratios. (a) $\widetilde{r}_0 = 0$, (b) $\widetilde{r}_0 = 0.4$, and (c) $\widetilde{r}_0 = 0.8$.

By combining Fig. 16(a)–(c), the contribution of $\widetilde{r}_0$ to the initial static stress conditions, blasting peak points, and the maximum and minimum dynamic circumferential stress points under different in-situ stress conditions can be compared.

5 Laboratory model experiments and result analysis

Laboratory contour blasting experiments are conducted on granite specimens measuring 200 mm × 200 mm × 50 mm under biaxial stress conditions with internal radius

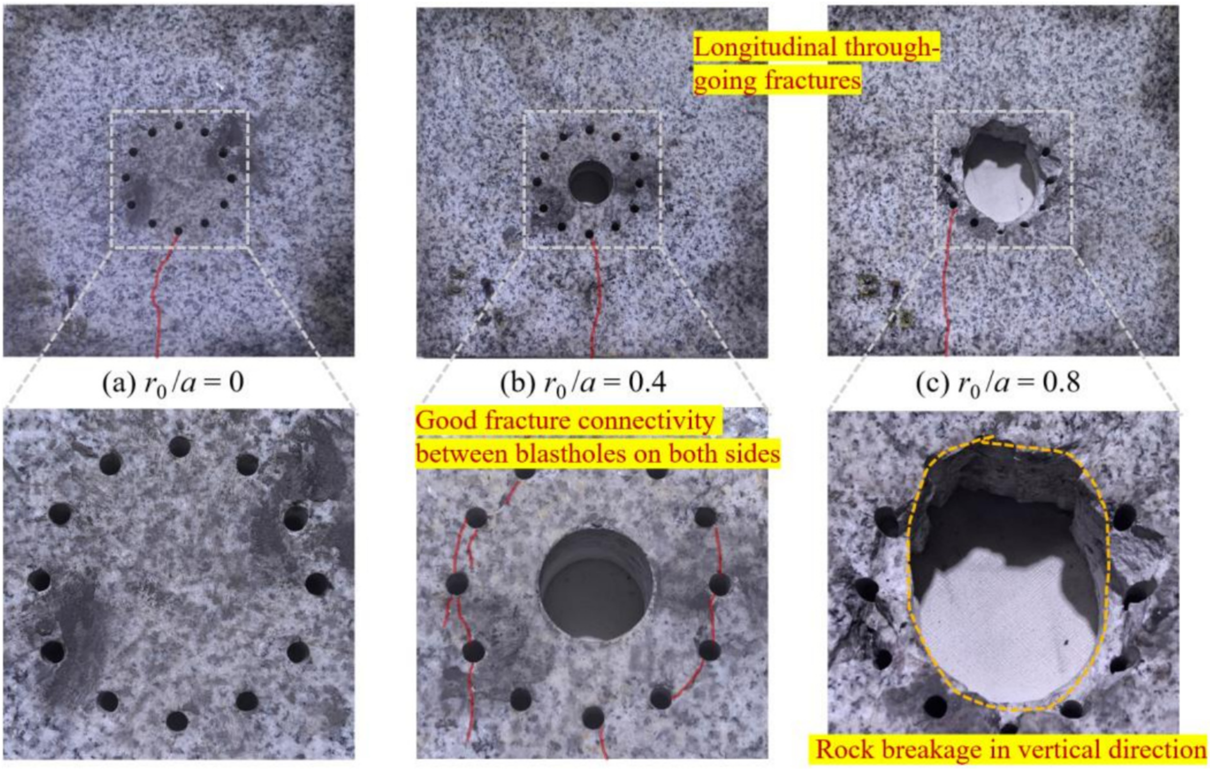

Fig. 20. Failure patterns after blasting under $\sigma_{\mathrm{v}} = 40$ MPa and $\sigma_{\mathrm{h}} = 0$ MPa with different internal radius ratios. (a) $\widetilde{r}_0 = 0$, (b) $\widetilde{r}_0 = 0.4$, and (c) $\widetilde{r}_0 = 0.8$.

ratios $\widetilde{r}_0 = r_0/a$ of 0, 0.4, and 0.8. The granite has a density of 3228 kg/m^3, P-wave velocity of 3914 m/s, and uniaxial compressive strength of 101 MPa. Twelve blastholes with a diameter of 4 mm are drilled uniformly along a 60 mm diameter circular tunnel profile. The charging structure consists of cement and black powder with a density of 790 kg/m^3 (Liu et al., 2024), composed primarily of potassium nitrate, charcoal, and sulfur, initiated by a blasting fuse as shown in Fig. 17.

Figure 18 illustrates the custom biaxial loading system used for static loading during blasting experiments, consisting of hydraulic pumps, jacks, rigid plates, and steel frames, along with a detonation system that connects twelve parallel blasting fuses to lead wires and battery cases. During the experiment, the specimen is positioned between loading plates with the blasting fuses connected to the detonation system, ensuring batteries remain disconnected during setup for safety. Static loading initiates via hydraulic pumps delivering high-pressure oil to jacks, controlled through pressure gauges. The process first applies equal biaxial stress, then increases the dominant component to the target state. Operators subsequently trigger detonation from a safe distance before documenting specimen failure patterns.

Figure 19 displays blast-induced failure patterns under zero static stress for varying $\widetilde{r}_0$. Without confining pressure, specimens exhibit multiple through-going fractures in random orientations, demonstrating extensive influence zones. At $\widetilde{r}_0 = 0$, blastholes show limited fracture connectivity. Increasing $\widetilde{r}_0$ enhances inter-hole fracture connectivity while intensifying interior fragmentation. When $\widetilde{r}_0 = 0.8$, an excavation boundary is successfully formed.

Figure 20 displays the failure patterns after blasting under $\sigma_{\mathrm{v}} = 40$ MPa and $\sigma_{\mathrm{h}} = 0$ MPa for different $\widetilde{r}_0$. All specimens exhibit a vertical through-going fracture. Comparison with Fig. 19 demonstrates that confinement pressure under varying k exerts directional control over fracture propagation, aligning with theoretical and experimental results (Li et al., 2024a; Liu et al., 2024). Furthermore, when $\widetilde{r}_0 = 0.4$, superior fracture connectivity is observed between the left and right sidewall blastholes. However, as $\widetilde{r}_0$ increases to 0.8, contour blasting preferentially induces rock breakage in the vertical direction. This phenomenon can be explained by the theoretical analysis: when $k = 0$ and $\widetilde{r}_0 = 0.8$, both radial and tangential stresses of surrounding rock along the vertical direction are low, thus providing insufficient confinement against blasting-induced failure. In contrast, when $\widetilde{r}_0 = 0.4$, the radial stress at the crown exceeds that at the sidewalls, as shown in Figs. 3(a) and 4(a), leading to preferential fracture linkage between sidewall blastholes.

Figure 21 illustrates the failure patterns after blasting with $\widetilde{r}_0 = 0.8$ under different k. With increasing k, vertical through-going fractures disappear. Meanwhile, the pattern of internal rock breakage evolves with increasing k: from an elliptical shape with its major axis aligned with the

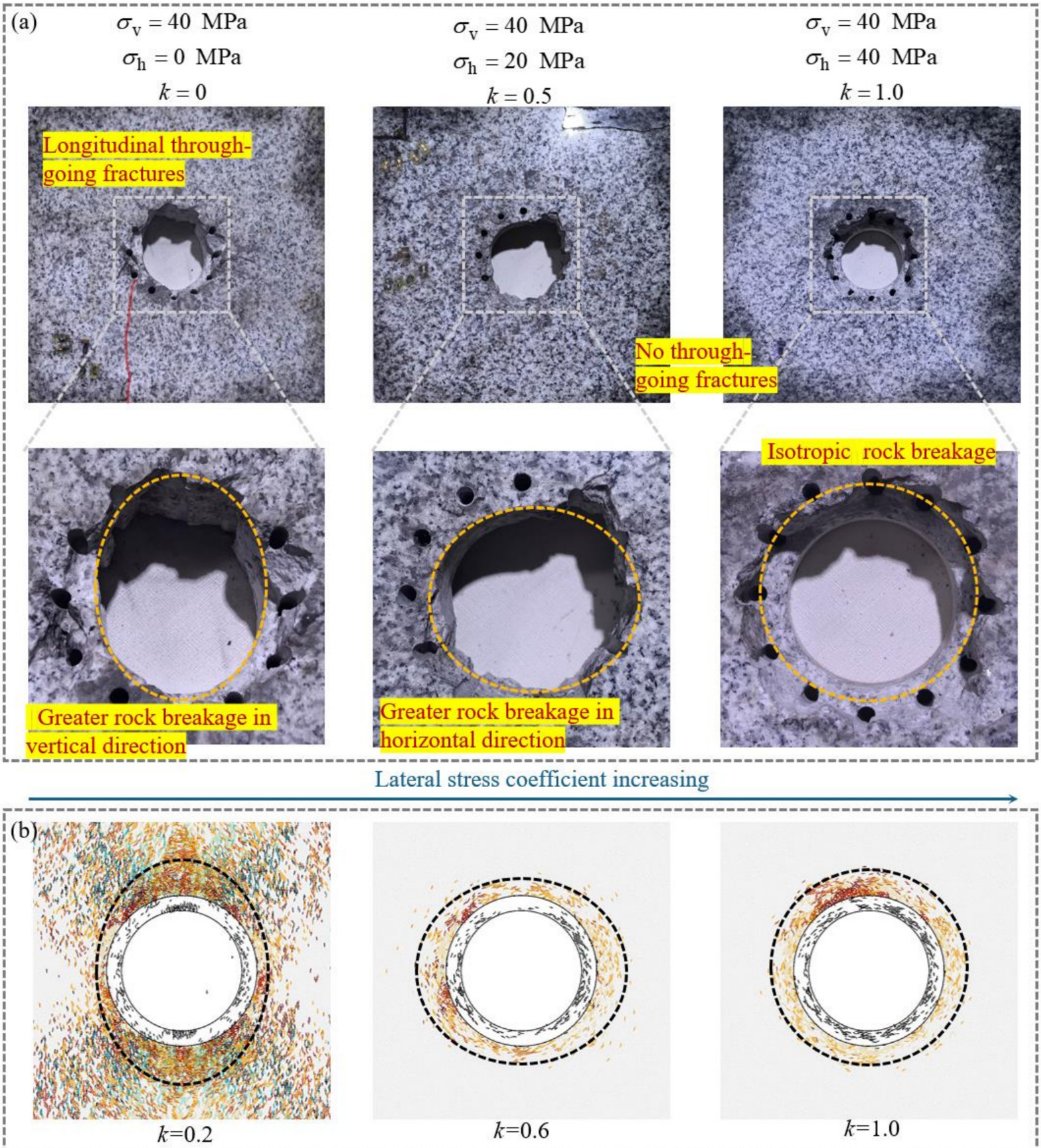

Fig. 21. Failure patterns after blasting under different k with internal radius ratios $\tilde{r}_0 = 0.8$. (a) Laboratory experiments, and (b) numerical simulations.

maximum principal stress, to one perpendicular to it, and eventually to a nearly circular shape when k reaches 1. These patterns match numerical simulations of fracture zone distributions and align with theoretical predictions.

In conclusion, the experimental results in this section are generally consistent with the previous analysis. It should be noted that the comparative validation in this section primarily addresses the qualitative conclusions regarding the adjustment of the static stress field with changes in the internal radius ratio and the relative influence of blasting pressure on failure characteristics.

6 Discussion

A mathematical-physical model is developed to analyze the dynamic response around deep tunnels during contour blasting-unloading under anisotropic stresses with varying $\tilde{r}_0$. The model characterizes stress evolution, enabling failure mechanism analysis at arbitrary surrounding rock locations.

As illustrated in Fig. 22(a), the combined evolution of unloading stress and blasting stress results in the blasting-unloading stress evolution (with the same coordinate sys-

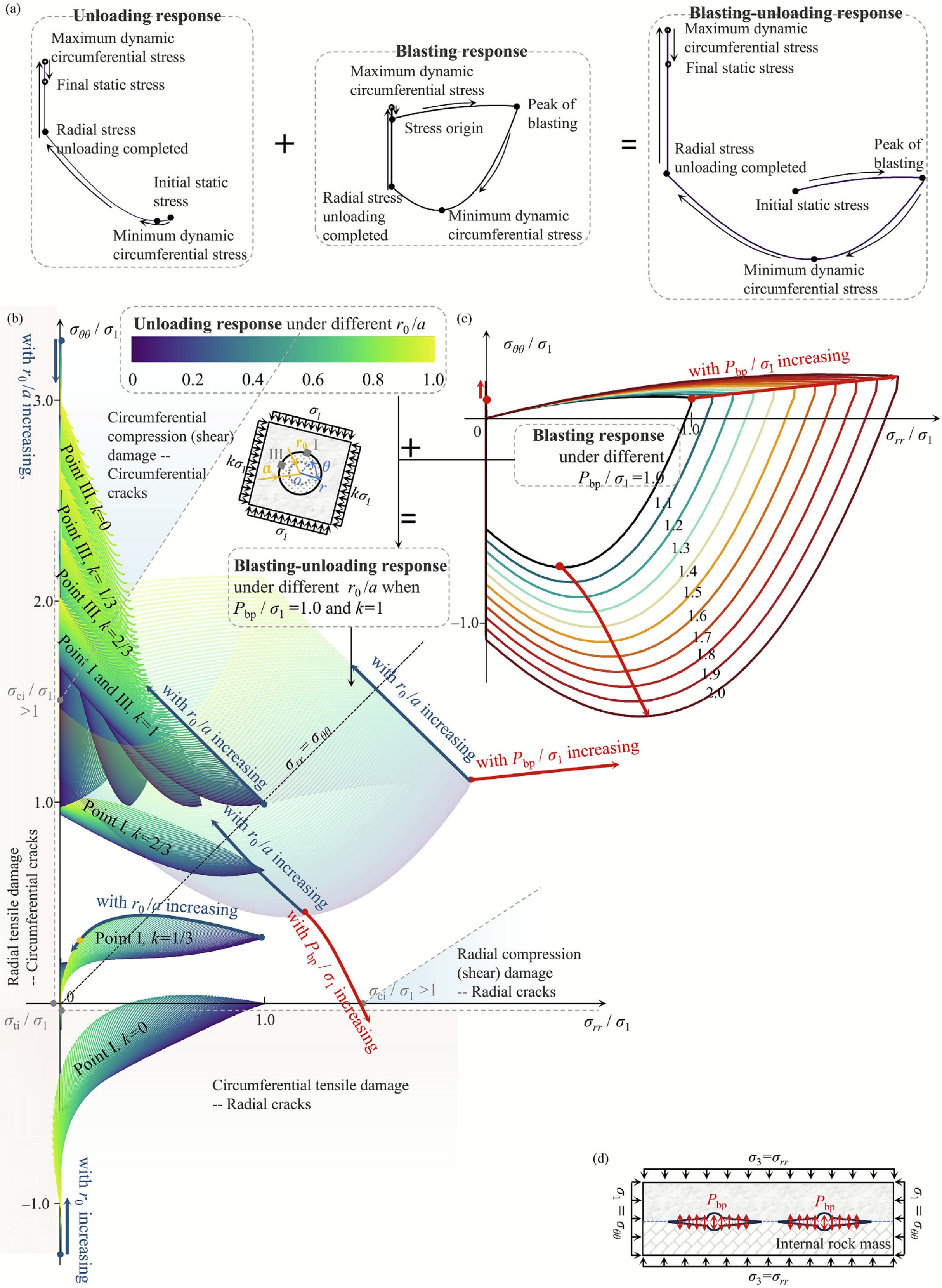

Fig. 22. Evolution of radial stress and circumferential stress. (a) Superposition of dynamic stress evolution induced by blasting and unloading, (b) dynamic stress evolutions induced by unloading under different static stress conditions, (c) dynamic stress evolutions induced by blasting under different peak blasting pressures, and (d) force state of the model at the tunnel contour.

tem as in Fig. 22(b)). The variation in $\widetilde{r}_0$ primarily affects the evolution of unloading stress, and this influence exhibits significant differences under varying k, as shown in the unloading response illustrated in Fig. 22(b). When the maximum and minimum principal in-situ stresses (σ_1 and σ_3) are known, the unloading response at the tunnel boundary — specifically at point I (aligned with σ_1) and point III (aligned with σ_3) — can be extracted from this figure. The evolution of blasting stress with varying peak of blasting pressure is shown in Fig. 22(c). As illustrated in Fig. 22 (c), the maximum radial stress of blasting response increases while the minimum circumferential compressive stress decreases with increasing blasting peak stress ratio (P_{bp}/σ_1). When the blasting response superimposes with the unloading response, the resulting dynamic stress may potentially enter either the radial compressive-shear failure region or the circumferential tensile failure region, as indicated by red arrows in Fig. 22(b). The spatial extent of the tensile failure region (marked in red) and the boundaries of the compressive failure region (shown in blue) are governed by the tensile crack initiation threshold σ_{ti} and the compressive-shear crack initiation threshold σ_{ci}, respectively. The failure behavior of surrounding rock, including both the occurrence and specific failure mode, is essentially determined by the competitive relationship between the superimposed blasting unloading response and the inherent strength thresholds of rock mass.

In practical construction, the in-situ stresses cannot be altered. However, by appropriately designing the blasting method and sequence, it is possible to achieve a smooth blasting contour while minimizing damage to the surrounding rock (Hustrulid, 1999). Taking a lateral stress coefficient of 2/3 as an example, as shown in Fig. 22(b), an increase in the internal radius ratio can effectively adjust the initial static stress of the surrounding rock parallel to the principal stress direction, resulting in circumferential stress exceeding radial stress (above the dashed line $\sigma_{rr} = \sigma_{\theta\theta}$ in Fig. 22(b)). This adjustment facilitates the formation of a smoother contour (Li et al., 2024b). According to Fig. 22(b), increasing $\widetilde{r}_0$ shifts the point of blasting peak to the left and raises the minimum dynamic circumferential stress, moving them away from the region where radial cracks may form. Based on the mechanical parameters of the surrounding rock estimated from experiments and field investigations, the specific locations of shear and tensile failure region can be determined in Fig. 22(b). When failure cannot be avoided through effective design, the failure pattern and extent of the surrounding rock can be assessed by analyzing the failure region through which the stress response passes, identifying whether radial or circumferential cracks are formed, and subsequently guiding support design. In cases where the failure conditions at a specific location need to be evaluated, the time-dependent evolution of the 2D stress matrix in polar coordinates can be obtained using the solution method proposed, which can then be converted into local maximum and minimum principal stresses and their directions (Boresi et al., 2010) for failure analysis.

It is necessary to note that a uniform blasting stress peak was adopted to control variables and compare the failure extent under varying $\widetilde{r}_0$ in this study. In fact, as $\widetilde{r}_0$ increases, the radial compressive stress on the blasting contour decreases while the circumferential pressure increases. For the blastholes located at the tunnel boundary, the stress distribution, as shown in Fig. 22(d), is formed. When σ_{rr} in Fig. 22(d) approaches zero, the compressive stress on the connecting line between boreholes decreases, even turning into tensile stress. This facilitates the generation of tensile cracks along the borehole alignment, thereby preserving the contour integrity while reducing the explosive charge (Persson et al., 1994). Additionally, a smaller charge leads to less disturbance to the surrounding rock. As demonstrated by the laboratory experimental results in Fig. 20 (b), under identical blast charge conditions, fractures between blastholes on both sides (with smaller radial stresses) exhibit better connectivity compared to those in the upper and lower regions (subject to higher radial stresses).

In previous discussions, it appeared that increasing the internal radius ratio is generally more beneficial. However, when the lateral stress coefficient is small, as shown by the unloading response of point I when $k = 1/3$ in Fig. 22(b), increasing $\widetilde{r}_0$ causes the initial circumferential stress to first increase and then decrease. Since circumferential stress provides protective confining pressure during blasting (Yang et al., 2018), and based on the results in Fig. 4(c), an internal radius ratio of approximately 0.82 may offer greater tolerance for blasting design. Moreover, when considering development blasting for the entire cross-section, it is not always optimal to simply increase the $\widetilde{r}_0$, as this would require more blasting rings and additional procedures (Bhandari, 1997), potentially leading to repeated damage to the surrounding rock.

The dynamic blasting-unloading stress evolution and its relationship with $\widetilde{r}_0$ apply not only to contour blasting but also serve as a guide for blast design in tunnel development. Moreover, this model can be further extended, such as by incorporating different blasting-unloading stress paths to more accurately capture the effects of nonlinear paths, utilizing conformal mapping to study the influence of different cross-sectional shapes (Liang et al., 2024a), and introducing damage constitutive models related to dynamic rates to investigate the cumulative damage from multiple full-section blasts, among others.

7 Conclusions

This study investigates dynamic stress evolution during tunnel contour blasting with varying internal radius ratios $\widetilde{r}_0$ through theoretical analysis, numerical simulation, and laboratory experiments, revealing the failure characteristics and mechanisms. Key findings include:

(1) For most in-situ stress conditions, increasing the internal radius ratio $\widetilde{r}_0$ typically reduces surrounding rock failure by modifying initial static stresses: decreasing radial stress while increasing circumferential stress. During blasting, the peak radial stress in the surrounding rock is reduced, resulting in less compressive shear failure; the total additional circumferential tensile stresses are reduced, thereby reducing the potential for circumferential tensile failure. These effects are significant at low-stress levels, reducing the overall blast-dominated radial fractures. During the unloading process, the unloading amplitude decreases due to the pre-release of the internal rock mass, thereby reducing the dynamic additional circumferential compressive stresses induced by unloading.

(2) Specifically, when k is less than 0.5, the circumferential stress at the tunnel boundary in the direction of the maximum principal stress decreases with increasing $\widetilde{r}_0$. When $0.2 < k < 0.5$, the circumferential stress decreases more slowly than the radial stress. Thus, by increasing $\widetilde{r}_0$, the static stress can be adjusted such that the circumferential stress exceeds the radial stress. By appropriately designing $\widetilde{r}_0$ and reducing the blasting pressure, the damage to the surrounding rock can be minimized while facilitating crack connection between the blastholes. Conversely, for $k < 0.2$, any adjustments to $\widetilde{r}_0$ will not preferentially direct blasting-induced cracks along the tunnel contour. Instead, fractures will continue to propagate radially along the maximum principal stress direction.

Data availability

The data that support the findings of this study are available from the corresponding author upon reasonable request.

CRediT authorship contribution statement

Siyu Peng: Writing – original draft, Visualization, Validation, Software, Methodology, Formal analysis, Conceptualization. **Xibing Li:** Supervision, Project administration, Funding acquisition. **Lisha Liang:** Software, Conceptualization. **Jingyao Gao:** Writing – review & editing.

Declaration of competing interest

The authors declare that they have no known competing financial interests or personal relationships that could have appeared to influence the work reported in this paper.

Acknowledgement

The research was supported by the National Natural Science Foundation of China (Grant Nos. 51927808 and 52434006) and the Postgraduate Innovation Fund Project of Hunan Province (Grant No. CX20200242). The financial supports are gratefully acknowledged.

References

Bhandari, S. (1997). *Engineering rock blasting operations*. A. A. Balkema.

Boresi, A., Chong, K., & Lee, J. (2010). *Elasticity in Engineering Mechanics*. Wileyhttps://books.google.co.jp/books?id=NEhdMVEX17oC.

Cao, W., & Younis, R. M. (2024). Empirical scaling of formation fracturing by high-energy impulsive mechanical loads. *International Journal of Rock Mechanics and Mining Sciences, 173*, 105613.

Carter, J. P., & Booker, J. R. (1990). Sudden excavation of a long circular tunnel in elastic ground. *International Journal of Rock Mechanics and Mining Sciences & Geomechanics Abstracts, 27*(2), 129–132.

Feng, X. T., Xu, H., Qiu, S. L., Li, S. J., Yang, C. X., Guo, H. S., Cheng, Y., & Gao, Y. H. (2018). In situ observation of rock spalling in the deep tunnels of the China Jinping underground laboratory (2400 m depth). *Rock Mechanics and Rock Engineering, 51*(4), 1193–1213.

Goodman, R. E. (1991). *Introduction to Rock Mechanics*. Wileyhttps://books.google.co.jp/books?id=9lK5EAAAQBAJ.

Hustrulid, W. A. (1999). *Blasting principles for open pit mining*. CRC Press.

Jiang, Q., Feng, X. T., Chen, J., Huang, K., & Jiang, Y. (2013). Estimating in-situ rock stress from spalling veins: A case study. *Engineering Geology, 152*(1), 38–47.

Kirsch, C. (1898). Die theorie der elastizitat und die bedurfnisse der festigkeitslehre. *Zeitschrift des Vereines Deutscher Ingenieure, 42*, 797–807.

Li, C. J., & Li, X. B. (2018). Influence of wavelength-to-tunnel-diameter ratio on dynamic response of underground tunnels subjected to blasting loads. *International Journal of Rock Mechanics and Mining Sciences, 112*, 323–338.

Li, C. J., Li, X. B., & Liang, L. S. (2020). Dynamic response of existing tunnel under cylindrical unloading wave. *International Journal of Rock Mechanics and Mining Sciences, 131*, 104342.

Li, S. J., Feng, X. T., Li, Z. H., Chen, B. R., Zhang, C. Q., & Zhou, H. (2012). In situ monitoring of rockburst nucleation and evolution in the deeply buried tunnels of Jinping II hydropower station. *Engineering Geology, 137–138*, 85–96.

Li, S. C., Wang, H. P., Qian, Q. H., Li, S. C., Fan, Q. Z., Yuan, L., Xue, J. H., & Zhang, Q. S. (2008). In-situ monitoring research on zonal disintegration of surrounding rock mass in deep mine roadways. *Chinese Journal of Rock Mechanics and Engineering, 27*(8), 1545–1553 (in Chinese).

Li, X. B., Cao, W. Z., Zhou, Z. L., & Zou, Y. (2014). Influence of stress path on excavation unloading response. *Tunnelling and Underground Space Technology, 42*, 237–246.

Li, X. B., Chen, J. Z., Ma, C. D., Huang, L. Q., Li, C. J., Zhang, J., & Zhao, Y. Z. (2022). A novel in-situ stress measurement method incorporating non-oriented core ground re-orientation and acoustic emission: A case study of a deep borehole. *International Journal of Rock Mechanics and Mining Sciences, 152*, 105079.

Li, X. B., Gong, F. Q., Tao, M., Dong, L. J., Du, K., Ma, C. D., Zhou, Z. L., & Yin, T. B. (2017). Failure mechanism and coupled static-dynamic loading theory in deep hard rock mining: A review. *Journal of Rock Mechanics and Geotechnical Engineering, 9*(4), 767–782.

Li, X. D., Liu, K. W., Sha, Y. Y., Yang, J. C., & Hong, Z. X. (2024a). Experimental and numerical investigation on rock fracturing in tunnel contour blasting under initial stress. *International Journal of Impact Engineering, 185*, 104844.

Li, X. D., Liu, K. W., Zhao, X. R., Sha, Y. Y., Yang, J. C., Ma, S. Z., & Hong, Z. X. (2024b). Study on rock fracturing in smooth blasting under initial stress. *Engineering Fracture Mechanics, 296*, 109865.

Li, X. H., Zhu, Z. M., Wang, M., Wan, D. Y., Zhou, L., & Liu, R. F. (2021). Numerical study on the behavior of blasting in deep rock masses. *Tunnelling and Underground Space Technology, 113*, 103968.

Liang, L. S., Li, X. B., Liu, Z. X., & Peng, S. Y. (2024a). Dynamic responses of U-shaped caverns under transient stress waves in deep rock engineering. *Mathematics, 12*(12), 1836.

Liang, L. S., Li, X. B., Zhu, Q. Q., Peng, S. Y., & Si, X. F. (2024b). Stress distribution and failure characteristics around U-shaped caverns with different height-to-width ratios under biaxial compression. *Engineering Failure Analysis, 156*, 107800.

Lin, P., Liu, H. Y., & Zhou, W. Y. (2015). Experimental study on failure behaviour of deep tunnels under high in-situ stresses. *Tunnelling and Underground Space Technology, 46*, 28–45.

Liu, H. L., Huang, L. Q., Wang, Z. W., Wu, Y. C., & Li, X. B. (2024). Experimental study on dynamic response of hard rock blasting under in-situ stress. *International Journal of Rock Mechanics and Mining Sciences, 182*, 105860.

Lu, W. B., Yang, J. H., Yan, P., Chen, M., Zhou, C. B., Luo, Y., & Jin, L. (2012). Dynamic response of rock mass induced by the transient release of in-situ stress. *International Journal of Rock Mechanics and Mining Sciences, 53*, 129–141.

Miklowitz, J. (1978). *The theory of elastic waves and waveguides*. North Holland Publishing Company.

Peng, S. Y., Li, X. B., Gao, J. Y., & Liang, L. S. (2024a). Energy evolution and failure mechanism of tunnel dynamic unloading in deep rock mass abounding in closable minor joints. *Tunnelling and Underground Space Technology, 154*, 106132.

Peng, S. Y., Li, X. B., Li, C. J., Liang, L. S., & Huang, L. Q. (2024b). Crack-closure behavior and stress-sensitive wave velocity of hard rock based on flat-joint model in particle-flow-code (PFC) modeling. *Computers and Geotechnics, 170*, 106320.

Peng, S. Y., Li, X. B., Mitani, Y., & Gao, J. Y. (2025). Multiple-stage dynamic responses and failure behaviors of surrounding rocks subjected to development blasting: Exponential and triangular paths. *Journal of Rock Mechanics and Geotechnical Engineering, 17*(6), 3773–3789.

Persson, P. A., Holmberg, R., & Lee, J. (1994). *Rock blasting and explosives engineering*. CRC Press.

Read, R. S., Chandler, N. A., & Dzik, E. J. (1998). In situ strength criteria for tunnel design in highly-stressed rock masses. *International Journal of Rock Mechanics and Mining Sciences, 35*(3), 261–278.

Si, X. F., Li, X. B., Gong, F. Q., Huang, L. Q., & Liu, X. L. (2022). Experimental investigation of failure process and characteristics in circular tunnels under different stress states and internal unloading conditions. *International Journal of Rock Mechanics and Mining Sciences, 154*, 105116.

Su, G. S., Chen, Y. X., Jiang, Q., Li, C. J., & Cai, W. (2023). Spalling failure of deep hard rock caverns. *Journal of Rock Mechanics and Geotechnical Engineering, 15*(8), 2083–2104.

Svanholm, B. O., Persson, P. A., & Larsson, B. (1978). Smooth blasting for reliable underground openings. In *Proceedings of the First International Symposium* (pp. 573–579).

Tao, J., Yang, X. G., Li, H. T., Zhou, J. W., Fan, G., & Lu, G. D. (2020). Effects of in-situ stresses on dynamic rock responses under blast loading. *Mechanics of Materials, 145*, 103374.

Yang, J. P., Chen, W. Z., Zhao, W. S., Tan, X. J., Tian, H. M., Yang, D. S., & Ma, C. S. (2017a). Geohazards of tunnel excavation in interbedded layers under high in situ stress. *Engineering Geology, 230*, 11–22.

Yang, J. H., Jiang, Q. H., Zhang, Q. B., & Zhao, J. (2018). Dynamic stress adjustment and rock damage during blasting excavation in a deep-buried circular tunnel. *Tunnelling and Underground Space Technology, 71*, 591–604.

Yang, J. H., Yao, C., Jiang, Q. H., Lu, W. B., & Jiang, S. H. (2017b). 2D numerical analysis of rock damage induced by dynamic in-situ stress redistribution and blast loading in underground blasting excavation. *Tunnelling and Underground Space Technology, 70*, 221–232.

Yi, C. P., Johansson, D., & Greberg, J. (2018). Effects of in-situ stresses on the fracturing of rock by blasting. *Computers and Geotechnics, 104*, 321–330.

Yilmaz, O., & Unlu, T. (2013). Three-dimensional numerical rock damage analysis under blasting load. *Tunnelling and Underground Space Technology, 38*, 266–278.

Zhao, R., Tao, M., Zhao, H. T., Wu, C. Q., & Cao, W. Z. (2023). Theoretical study on dynamic stress redistribution around circular tunnel with different unloading paths. *Computers and Geotechnics, 163*, 105737.

Zhou, J., Zhang, Y. L., Li, C. Q., He, H. N., & Li, X. B. (2024). Rockburst prediction and prevention in underground space excavation. *Underground Space, 14*, 70–98.

Zhu, H. H., Yan, J. X., & Liang, W. H. (2019a). Challenges and development prospects of ultra-long and ultra-deep mountain tunnels. *Engineering, 5*(3), 384–392.

Zhu, J. B., Li, Y. S., Peng, Q., Deng, X. F., Gao, M. Z., & Zhang, J. G. (2021). Stress wave propagation across jointed rock mass under dynamic extension and its effect on dynamic response and supporting of underground opening. *Tunnelling and Underground Space Technology, 108*, 103648.

Zhu, Q. Q., Li, C. J., Li, X. B., Li, D. Y., Wang, W. H., & Chen, J. Z. (2022). Fracture mechanism and energy evolution of sandstone with a circular inclusion. *International Journal of Rock Mechanics and Mining Sciences, 155*, 105139.

Zhu, Q. Q., Li, D. Y., Han, Z. Y., Li, X. B., & Zhou, Z. L. (2019b). Mechanical properties and fracture evolution of sandstone specimens containing different inclusions under uniaxial compression. *International Journal of Rock Mechanics and Mining Sciences, 115*, 33–47.

Zhu, W. C., Wei, J., Zhao, J., & Niu, L. L. (2014). 2D numerical simulation on excavation damaged zone induced by dynamic stress redistribution. *Tunnelling and Underground Space Technology, 43*, 315–326.